ALGORITHMS FOR IMAGE SEGMENTATION APPLIED TO DT-MR IMAGES AND MAMMOGRAMS

by

Saba El-Hilo
B.Sc., Queen's University, 2009

a Thesis submitted in partial fulfillment
of the requirements for the degree of
Master of Science
in the School
of
Computing Science

SIMON FRASER UNIVERSITY
Summer 2011

APPROVAL

Name: Saba El-Hilo

Degree: Master of Science

Title of Thesis: ALGORITHMS FOR IMAGE SEGMENTATION APPLIED TO DT-MR IMAGES AND MAMMOGRAMS

Examining Committee: Dr. Pavol Hell
Chair

Dr. Stella Atkins, Senior Supervisor,
Professor, Computing Science
Simon Fraser University

Dr. Mark S. Drew , Supervisor,
Professor, Computing Science,
Simon Fraser University

Dr. Mirza Faisal Beg, Examiner
Associate Professor, Engineering Science
Simon Fraser University

Date Approved: 21 July 2011

Declaration of
Partial Copyright Licence

Abstract

An important and crucial part of any object oriented image processing procedure is successful image segmentation which, is a method of separating an image into regions of interest. Our contributions are as follows: (i) We propose a novel method to apply the random walker method to segment non-scalar diffusion tensor magnetic resonance imaging (DT-MRI) data. We also extend the implementation by including a non-parametric probability density model to enable the random walker method to successfully segment disconnected objects. (ii) We apply the random walker method to both 2^{nd} and 4^{th} order DT-MR data and demonstrate the advantages of performing segmentations on higher order data. (iii) We use a DTI segmented atlas to investigate tissue discrimination in the brain, which serves to evaluate a measure of diffusion anisotropy (iv) Finally, we propose a novel method for the segmentation of the breast from mammograms. The method automatically identifies intensity values that are used to define a probability distribution used in the segmentation.

Keywords: segmentation; random walker; diffusion tensor magnetic resonance imaging (DT-MRI); probability density; fourth order; anisotropy; mammograms; medical image analysis

Subject Terms: medical image analysis; segmentation

To my family.

"The most exciting phrase to hear in science, the one that heralds the most discoveries, is not Eureka! but 'That's funny...'"

—Isaac Asimov, (1920-1992)

"Keep your eyes on the stars and your feet on the ground"

— Theodore Roosevelt, (1858-1919)

Acknowledgments

The work done in this thesis would not have been possible without the generous support I received from many people surrounding me. First, I would like to sincerely thank Dr. Stella Atkins, my senior supervisor for her encouragement, intellectual support and guidance. She supported this work with her valuable time, ideas and skills and made several collaborations with the wider research community possible. I am extremely grateful for her trust in my work and abilities, unwavering support and hard work. I am also grateful for her help with regards to obtaining an internship position in the medical image analysis research field (McKesson) and her valuable career advice.

I also wish to acknowledge and thank Dr. Mahmoud Ramze Rezaee for his support and guidance while working at Mckesson. He gave me a new perspective on medical imaging analysis and made it possible to see how our research in the lab can be applied to the health care sector. Moreover, I thank him for all the discussions we had about segmentation methods and for his critical analysis of the mammogram segmentation approach we devised. I would also like to thank Mr.Cliff Edwards from Mckesson for his substantial time and efforts which also made the internship possible.

I would also like to thank a member of my supervisory committee, Dr. Mark Drew for his time and effort spent reading this work and for his helpful comments and constructive criticisms. His perspective on the mammogram segmentation problem allowed me to take a valuable second look at my approach which lead to some improvements. Moreover, I would like to thank Dr. Mirza Faisal Beg for inspiring me to rerun some the experiments which lead to more significant results.

I wish to extend a sincere thanks to all the lab members with whom I had the pleasure to spend time with during my graduate studies. I have gained much knowledge and experiences from my interaction with everyone in our lab. In particular I would like to thank Mr. Yonas

Tesfazghi Weldeselassie for his guidance and assistance with regards to getting me up to speed in the area of DT-MRI.

Finally, I would like to thank my family for their endless support throughout my graduate studies. I thank my parents for their patience, love and guidance. I am grateful for the passion and attention they have always showed in anything I have done and especially with regards to developing this work.

Contents

List of Tables

List of Figures

Chapter 1

Introduction

Diffusion tensor magnetic resonance imaging (DT-MRI) has attracted attention in many fields such as image processing, computer vision, and medical imaging. To this date, it remains the only non invasive method that provides a mean of distinguishing between anatomical structures of the white matter in the brain. Unlike scalar images where each pixel is an intensity value, in DT-MR images each voxel is a 3x3 symmetric positive definite diffusion tensor depicting the anisotropy within the underlying tissue. The diffusion tensor depicts the degree of and the principle direction of anisotropic diffusion. Several Scalar measurements have been proposed to describe the properties of the diffusion tensor and its diffusion anisotropy[34].

Image segmentation can be described as the process of separating an image into regions of interest. Segmentation methods should be able to provide fast computation, avoid over segmentation and produce accurate and intuitive segmentations. The random walker segmentation method demonstrates those qualities[18]. Therefore, we choose to extend it to segment DT-MR images.

Segmentation tends to be the first essential and crucial step of most medical image analysis tasks, since once a region of interest is segmented, one can deduce shape, appearance and structural features about the region. These qualities in turn can be used for diagnosis aid or treatment evaluation. There are many applications of segmentation. For example, we develop a segmentation method for detecting the breast region in mammograms, which is the first step in a Computer-Aided Detection (CADe) process. Detecting the breast region allows the radiologist to automatically zoom in on the breast, hence removing the background and confining the area of which the radiologist should look at and diagnose.

Most segmentation techniques focus on providing automatic and unsupervised segmentations, by grouping elements according to a predefined criteria such as image intensity distribution or homogeneity. However, supervised segmentation has gained much attention in the field of computer vision. The reasoning is that these methods give users the ability to obtain the segmentation result as necessary for the application on hand. There are three general types of supervised segmentation methods: (i) The user provides points of the desired boundary which the algorithm completes. (ii) The user provides an entire contour or boundary that is close to the object's real boundary. The algorithm then evolves the boundary supplied by the user to include the object. (iii) The user provides an initial labeling of some pixels as belonging to the desired object to be segmented or to the background. The algorithm then labels the rest of the pixels appropriately. Correction of an inaccurate segmentation could be remedied by asking the user to supply more initial seed points.

The random walker segmentation algorithm can be classified under the third type of supervised segmentation algorithms. Although supervised segmentation algorithms have attractive qualities since they involve the user, they do tend to be more time consuming for the user and are not really practical when performing segmentation on a large number of images. Moreover, they can't be incorporated in automatic programs that require no user input, especially when the end user is a radiologist that needs to diagnose and view as many images as possible in a short time frame. It would be very impractical to involve such a user in a segmentation process.

1.1 Thesis Contribution

In this thesis we focus on the research and development of two segmentation approaches. One is a supervised segmentation approach applied to DT-MR images, and another is fully automatic and unsupervised, which is applied to mammograms. Moreover, we investigate the ability of anisotropy measures to distinguish between different types of brain tissue. Our contributions are as follows: (i) We propose a novel approach to apply the random walker segmentation method to segment non-scalar diffusion tensor magnetic resonance image (DT-MRI) data. We also extend the implementation by including a non-parametric probability density model to enable the random walker method to successfully segment disconnected objects. (ii) We apply the random walker method to both 2^{nd} and 4^{th} order DT-MR data and compare the results of both segmentation approaches. We demonstrate the advantages

of performing segmentations on higher order data. (iii) We use a DTI segmented atlas to investigate tissue discrimination in the brain, which serves to evaluate a measure of diffusion anisotropy. (iv) Finally, we propose a novel method for the segmentation of the breast area from mammograms.

Chapter 2

Background

2.1 Diffusion Tensor Magnetic Resonance Imaging

Conventional MRI allows us to identify the major functional centers of the brain (such as the cortex and nuclei). However, the white matter region in the brain appears homogeneous and provides no information about the complex arrangement of fiber tracts. On the other hand, DT-MRI allows the demonstration of anisotropic water diffusion in the brain and makes it possible to visualize the more complex arrangement of fibers and white matter structure.

A DT-MRI image voxel reflects the displacement distribution of the water molecules present within the voxel. The study of this displacement provides information about the structure and geometric organization of tissues. Molecular mobility and diffusion in tissues may not be the same in all directions. This anisotropic diffusion could be attributed to tissue structure or the presence of obstacles that limit molecular diffusion in a certain direction. In particular, axonal cell membranes and myelin sheaths can restrict the mobility of water. Thus, the measured DT becomes highly anisotropic and oriented in areas of compact nerve fiber organization [8]. This anisotropic nature of diffusion of water molecules in tissue can be described mathematically by a rank-2 tensor. Therefore each voxel of the imaging volume is a 2^{nd} order 3x3 symmetric positive definite matrix (diffusion tensor) which depicts the anisotropy within the tissue. The approximated diffusivity function is given by [20]

$$d\left(g\right) = g^T D g \tag{2.1}$$

where g=$[g_1, g_2, g_3]^T$ is the magnetic gradient direction and D is the estimated 2^{nd} order

tensor. In DT-MRI the diffusion weighted echo intensity image (DWI) S_l for different directions l are measured. These are related to the 3x3 diffusion tensor $\mathbf{D}$ through the Stejskal-Tanner equation

$$S_l = S_0 e^{-b_l:D} = S_0 e^{-\sum_{i=1}^{3}\sum_{j=1}^{3} b_{l,ij} D_{ij}} \tag{2.2}$$

where b_l is a diffusion weighting variable that corresponds to the l^{th} magnetic gradient, ":" is a generalized inner product for matrices. $\mathbf{D}$ can be estimated using multivariate regression techniques . Anisotropic diffusion can be described by the equation

$$\frac{\partial C}{\partial t} = \nabla \cdot (D \nabla C) \tag{2.3}$$

where C is the concentration of the water molecules and $\mathbf{D}$ is a diffusion coefficient which is the 3x3 symmetric second order tensor. The tensor fully describes molecular mobility along each direction:

$$D = \begin{bmatrix} D_{xx} & D_{xy} & D_{xz} \\ D_{yx} & D_{yy} & D_{yz} \\ D_{zx} & D_{zy} & D_{zz} \end{bmatrix} \tag{2.4}$$

Fig. 2.1 shows a "slice" of the diffusion tensor volume data of a human brain data set used in our experiments (from a publicly available DTI atlas (JHU MNI SS) downloaded from Johns Hopkins Medical Institute Laboratory of Brain Anatomical MRI (http://lbam.med.jhmi.edu/)). Each of the six independent components of the symmetric positive definite diffusion tensor presented in equation 2.4 is shown as a scalar image.

Anisotropic diffusion is best visualized as an ellipsoid where the radius defines the diffusion in a particular direction [34]. Fig. 2.2 shows a graphical representation of a hypothetical diffusion ellipsoid. The three axes of the ellipsoid (D1,D2,D3) represent the eigenvectors of the diffusion tensor, whereas the lengths of the axes (E1,E2,E3) are the eigenvalues.

The DT is interpreted by calculating its eigenvalues and eigenvectors. The eigenvector corresponding to the highest eigenvalue describes the direction of the principle diffusion. The eigenvalues $(\lambda_1, \lambda_2, \lambda_3)$ and the corresponding eigenvectors $(\hat{e_1}, \hat{e_2}, \hat{e_3})$ can be obtained by diagonalizing the 3x3 diffusion tensor. A tensor D can be formulated by its eigenvalues and eigenvectors [34].

$$D = (\hat{e_1}, \hat{e_2}, \hat{e_3}) \begin{bmatrix} \lambda_1 & 0 & 0 \\ 0 & \lambda_2 & 0 \\ 0 & 0 & \lambda_3 \end{bmatrix} (\hat{e_1}, \hat{e_2}, \hat{e_3})^T \tag{2.5}$$

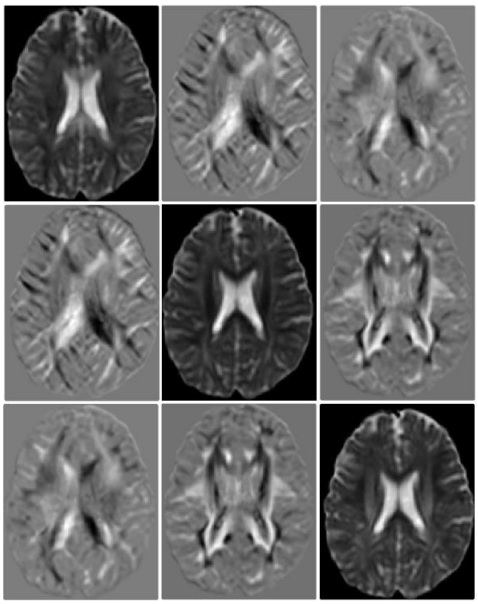

Figure 2.1: Slice of a tensor volume. Each sub-image in the image matrix corresponds to one component of the tensor D described in equation 2.4

The eigenvalues and eigenvectors of a diffusion tensor can be used to compute scalar diffusion anisotropy measures. These measures provide a scalar representation of the DT-MR images and describe the diffusion anisotropy. The significance of these measures is that they provide the ability to monitor changes in the anisotropic properties of white matter fiber bundles which could be caused by neurological diseases such as Multiple Sclerosis. Invariant indices are made of combinations of the diffusion tensor's eigenvalues. The most commonly used scalar diffusion anisotropy measure is fractional anisotropy (FA), which is used to approximate the diffusivity of water in tissue in vivo. FA values have a range of $[0, 1]$. Areas that are highly anisotropic have a larger value than areas that are isotropic.

2.2 Existing DTMRI Segmentation Methods

What makes the segmentation of DT-MR images a challenge is the use of an appropriate metric that can capture the difference or distance between diffusion tensors. When dealing with scalar images, the subtraction of one intensity value from another is sufficient to quantify the difference between two pixels. Such a metric should incorporate the whole

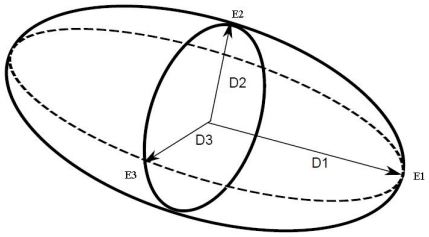

Figure 2.2: Graphical representation of a diffusion ellipsoid.

tensor information. Meaning, it should utilize both the eigenvalues and eigenvectors of the diffusion tensors.

Another challenge with the segmentation of DT-MRI data is the nature of the diffusion tensors. The diffusion matrix is not rotationally invariant so that the elements in the matrix do change with different orientations of the sample or field gradient. Therefore an invariant representation of a tensor that is independent of the frame of reference and the direction of the field's gradient is needed.

The method proposed by Zhukov et al[38] focuses on segmenting white matter regions in DT-MR images. They present an anisotropy measure that is rotationally invariant by only incorporating the eigenvalues, since the eigenvalues do not change after the rotation of the tensor's frame of reference. The anisotropy measure proposed C_a is defined as

$$C_a = \frac{1}{6}\left[\frac{\lambda_2+\lambda_3}{\lambda_1} + \frac{\lambda_1+\lambda_3}{\lambda_2} + \frac{\lambda_1+\lambda_2}{\lambda_3}\right] \tag{2.6}$$

Two scalar volumes are then calculated. One, represents the total diffusivity within a voxel which is formed by calculating the trace of the tensor matrix. The second scalar volume is formed by using the anisotropy measure presented above. The segmentation is performed on these scalar volumes using a level set segmentation method. Therefore, the segmentation is performed on the scalar images and not on the full DT-MR images. The directional information contained in the tensors (eigenvectors) is ignored and is not part of the segmentation solution. Therefore, the algorithm fails to distinguish between regions which have the same diffusion anisotropy magnitude but different directions.

Wang and Vemuri [31] present a tensor distance that is invariant to rotation and uses both directions and magnitude of diffusion. This tensor distance is incorporated into the

active contour model "without edges". The tensor distance metric defined follows the physical phenomenon of diffusion, is affine invariant and computationally tractable. By using this metric instead of of relying only on either the eigenvalues or eigenvectors, their method makes use of all the information contained in the tensor. The metric is incorporated in a level set framework to perform the segmentations. However, the nature of the active contour method that is used makes this segmentation approach unattractive. Active contours tend to be very sensitive to parameter initialization and runs into the risk of finding suboptimal solutions.

Weldeselassie and Hamarneh[33] also use the whole tensor information to perform segmentation on DT-MRI using a graph cuts approach. They use the affine invariant metric proposed by Wang and Vermuri. They also use the Log Euclidean distance metric to capture the difference between diffusion tensors. These measures are then incorporated in the graph cuts segmentation method. However, the graph cuts segmentation method suffers from the small cut problem. Since the method tries to minimize the sum of the edge weight in the cut, very small segmentations could be produced. Moreover, it doesn't extend easily to more than two labels.

2.3 Brain Tissue Discrimination

The anisotropy of the diffusion tensor can be described as the degree to which the tensor deviates from the isotropic case. Measures of diffusion anisotropy reduce the shape description of the 3D tensor to a scalar value that can be used to describe the tensor's anisotropy[3].

The degree of diffusion tensor anisotropy is associated with the structure of brain tissue. For instance, white matter in the brain is anisotropic whereas gray matter displays no anisotropy and can be described as isotropic. There are several measures of diffusion anisotropy that have been proposed, such as fractional anisotropy (FA), relative anisotropy (RA) or shape anisotropy (SA). These measures provide us with the ability to distinguish between different types of tissue. Recent studies have shown that diffusion anisotropy can be used to investigate white matter morphology, white matter trauma and the development of white matter tracts in infants.

The measures of diffusion anisotropy all behave differently. Although, they all include various combinations of orthogonal diffusion measurements and rotationally invariant measures based upon the eigenvalues of the tensor. Thus, it is important to investigate the

relationship between these anisotropy measures and their ability to distinguish between brain tissue.

2.4 Breast Segmentation from Mammograms

Breast cancer is a major health problem in Western countries. It accounts for approximately 30% of all new cancer cases each year. Mammography is still the most commonly used method for detecting breast cancer. Detection of breast cancer at an early stage is a critical issue for a high survival rate [36].

Radiologists interpret the mammograms and attempt to identify areas of potential abnormalities. Therefore, the effectiveness of this screening method is dependent on the radiologist's ability to detect areas of subtle irregular abnormalities. It is estimated that between 10-30% of women diagnosed with breast cancer have false-negative mammograms [36]. Most of the false-negative cases can be attributed to the radiologist's failure to detect a cancer which could be due to misinterpretation, or simply that the radiologist overlooked the area. It has been demonstrated that an independent second reading can significantly improve the detection rate and decrease the number of false positive cases.

Computerized tools and analysis can act as an independent secondary reading. The tools can be described as a supplement or a "second reader" to assist the physician in detecting and diagnosing breast cancer. These tools can be classified into two different processes: Computer-Aided Detection (CADe) and Computer-Aided Diagnosis (CADi). Detection is the ability to identify abnormal areas in the breast, and diagnosis follows the detection process to identify those regions as being benign or malignant. Before these processes can perform their roles a really important pre-processing step has to take place which is the detection or segmentation of the breast region from the background.

The segmentation of the breast region is an important pre-processing step since it allows the search for abnormalities to be constricted to the breast region without influence from the background of the mammogram. However, the segmentation of the breast in mammograms can be a challenging problem because of several issues:

1. The breast air interface is a very low gradient that can be obscured with noise which makes edge detection a hard task.

2. Uncompressed fat near the breast air interface is a gradient, growing as the fat nears

the center of the breast. So there are no big areas of uniform intensity.

3. The background of the mammograms can be noisy especially if the mammograms are scanned in.

4. Some mammograms contain artifacts such as labels, wedges and scratches that can be hard to separate from the breast area.

2.5 Thesis Outline

The rest of the thesis is organized as follows,

- In Chapter 3, we present the introduction, methods, results and discussion of the extension of the random walker segmentation algorithm to 2^{nd} order DT-MR images.
- In Chapter 4, we present the introduction, literature review, results and discussion on the comparison between segmentations performed on 2^{nd} and 4^{th} order DT-MRI data.
- In Chapter 5, we present the introduction, methods, results and discussion on the discrimination of brain tissue.
- In Chapter 6, we present the introduction, methods, results and discussion on the developed novel segmentation framework for mammograms.
- In Chapter 7, we conclude and summarize our thesis and contributions.

Chapter 3

DT-MRI Segmentation Using Random Walker

3.1 Introduction

Tissue segmentation and classification performed on DT-MRI has several advantages over other modalities such as conventional MRI. Diffusion data provides us with physical information about the internal structure of the tissue scanned. Existing segmentation approaches on DT-MR images suffer from several problems. For instance, ignoring the directional information contained in the tensors leads to the failure to distinguish between regions which have the same diffusion magnitude but different directions. To obtain a meaningful and robust segmentation, all of the information provided by the tensor should be considered. Meaning, both the diffusion magnitude (eigenvalues) and direction (eigenvectors) should be incorporated in the segmentation approach.

The random walker segmentation technique has been successfully applied to scalar images. It is a segmentation technique that provides fast computation, avoids over segmentation and provides accurate and intuitive segmentations. The algorithm is an interactive segmentation technique, meaning it requires user input. Random walker provides a K-way image segmentation given user labeled voxels called seeds. Each seed is used to specify a region of interest which needs to be segmented [18].

A segmentation is produced on a weighted graph representation of the image. Nodes of the graph correspond to voxels in the image and edges are placed between neighboring

nodes. The edge weights are determined by a similarity measure so that a large weight corresponds to two very similar voxels and vice versa. The segmentation is produced on the graph by computing the probability that a random walker starting its walk at a voxel first reaches a seed with a label. Each voxel in the image is assigned the label with the greatest probability. What makes the random walker formulation especially attractive, is that the probabilities can be computed by solving a sparse, symmetric, positive-definite, system of linear equations instead of performing an actual random walk, since actually simulating random walks on images would be completely infeasible.

In [18] Grady demonstrates that the probability a random walker first reaches a seed point exactly equals the solution to the Dirichlet problem with boundary conditions at the locations of the seed points. Therefore when performing the segmentation, the seed points in question can be assigned to unity while all the other seed points can be assigned a value of zero. This establishes the concept of assigning voxels with a probability, where the seeds in question have the highest probability (one), the seeds of other labels have lowest probability (zero) and the rest of the voxels have values between one and zero.

Recently, the computer vision community has preferred spatial segmentation algorithms such as random walker, normalized cuts, graph cuts, active contours and level sets. This is because traditional statistical pattern recognition segmentation techniques could lead to small scattered, fragmented, noisy segmentations, since they don't take advantage of the spatial relationships between the pixels. However, sometimes the objects of interest can in fact be described by an appropriate feature distribution. Therefore, incorporating feature information into a spatial algorithm such as random walker, would lead to more accurate segmentations.

The random walker algorithm has been shown to have the following properties: (i) The solution for the probabilities is unique. (ii) It is guaranteed that each segment is connected to a seed point with some label. (iii) Only intensity gradients are used instead of considering feature informations. The second and third properties of the algorithm can be problematic for certain segmentation situations, specifically for the segmentation of images with many disconnected objects. To obtain a meaningful segmentation the user would have to seed each object individually.

The originally proposed random walker segmentation algorithm fails to segment regions of interest that are disconnected since, the algorithm is spatial and doesn't take advantage of any feature distribution. For many segmentation tasks this is sufficient and desirable.

Ignoring feature information removes the risk of having small scattered segmentations of small regions. However, incorporating probabilistic models of objects of interest allows the segmentation of disconnected objects. This results in an extended random walker algorithm that utilizes feature models obtained using a density estimation from seeds provided by the user [17].

Other algorithms have incorporated statistical information into a spatial approach. For instance, methods of segmentation that are based on minimizing an energy function add energy terms to the function that describe feature distribution. The graph cuts method has a "data term" which represents a prior distribution model [11]. The random walker and graph cuts algorithms obtain a segmentation by minimizing the same functional. However, the random walker algorithm minimizes the functional over a space of real numbers where the graph cuts approach minimizes over a space of integers. The segmentations obtained from the two algorithms have different properties and may produce different segmentation results on the same image.

The graph cuts method treats the foreground/background seeds as source/sink nodes for a max-flow/min-cut operation. A max-flow/min-cut algorithm is used to find a set of edges with a minimum weight which is then returned as the object's boundary. A common problem with the graph cuts approach is the "small cut" behavior. The reason behind this behavior is that the graph cuts will find the smallest cut between the seeds which results in a cut that doesn't fully enclose an area of defined seeds. This is especially the case with boundaries that are weakly defined, or when few seeds are placed. The method minimizes the total edge weights in the cut which could lead to very small segmentations. In [28] the authors present a segmentation framework that unifies both approaches and they show that the general algorithm can be made to behave like either the graph cuts method or the random walker by changing one parameter.

3.2 Contribution

In this chapter, we extend the random walker segmentation method using prior models to DT-MRI data. This work has been published as[15]. The DT-MRI data is converted to a graph where each tensor is a vertex and is connected to neighboring tensors by a weighted edge. Tensor distance metrics are used to asses the similarity between tensors and calculate the weights, since simply taking the Euclidean difference between the two tensors

doesn't give satisfactory results. Euclidean computations allow the presence of matrices with null or negative eigenvalues which physically don't make sense. Moreover, the euclidean averaging of tensors can lead to a tensor swelling effect which introduces dispersion to the computations. The two metrics used in our method are the Log-Euclidean and J-divergence tensor distance measures. The Log Euclidean tensor distance metric is also used to establish the tensor prior models.

Section 3.3.1 provides an overview of the random walker formulation and its extension to segment DT-MR images. In section 3.3.2 the incorporation of prior models into the random walker segmentation method is presented. Section 3.3.3 presents the tensor distance metrics used. Section 3.3.4 explains how the weights on the graph are calculated. The experimental segmentation results on both synthetic and real DT-MRI data is presented in section 3.4. A discussion and concluding remarks are made in section 3.5.

3.3 Methods

3.3.1 Random Walker Formulation

The segmentation is carried out on a weighted graph which is constructed from the image to be segmented. Each node represents a tensor voxel (T_i) from the DT-MR image. A graph consists of a pair G=(V,E) with vertices $v \in V$ and edges $e \in E$. An edge between two vertices v_i and v_j is referred to as e_{ij} . Let $n = |V|$ and $m = |E|$ where $|\cdot|$ denotes cardinality. Each edge is assigned a weight and is referred to as w_{ij}. The weights of the edges are computed using the tensor distance measures. The degree of a vertex is $d_i = \sum w(e_{ij})$ for all the edges e_{ij} incident to the vertex v_i.

The user provides a set of labeled voxels V_L with K labels which are referred to as seeds. For instance, the user can provide two types of labels (K=2): **object** and **background**, where the object label consists of the tensors that belong to the object to be segmented and the background label corresponds to the tensors that make up the background of the DT-MR image. The seeds are provided by asking the user to paint over a scalar image calculated from the original DT-MR image. The scalar image is formed using the trace of the DT-MRI dataset.

Given the graph and a set of labeled vertices, the goal of the random walker algorithm is to label each unlabeled vertex V_U in the graph with a label s provided by the user. Fig. 3.1 provides an illustration of how the graph is constructed from a DT-MR image. Ellipsoids

are used to visualize the diffusion tensors (voxels).

For each vertex $v_i \in V_U$ a probability x_i^s is calculated which represents the probability that a random walker starting from that vertex first reaches a labeled vertex $v_j \in V_L$ assigned to label s. The segmentation is then produced by labeling each vertex with the label for which it has the highest probability. To find the probability x_i^s that a random walker starting from a vertex v_i first reaches a labeled node, the following energy functional has to be minimized [18]

$$E = x_U^{sT} L x_U^s \tag{3.1}$$

x^s is a nx1 vector defined over the set of all nodes. It gives the probability x_i^s that a random walker starting from node v_i first reaches a labeled node with label s. This labeled node has a value of $x_i^s = 1$. L represents the combinatorial Laplacian matrix defined as

$$L_{v_i,v_j} = \begin{cases} deg_{v_i} & \text{if } i = j \\ -w_{ij} & \text{if } v_i \text{ and } v_j \text{ are adjacent vertices} \\ 0 & \text{otherwise} \end{cases} \tag{3.2}$$

where deg_{v_i} is the degree of the vertex v_i. The Laplacian matrix can be partitioned into labeled (L) and unlabeled (U) vertices

$$L = \begin{bmatrix} L_L & B \\ B^T & L_U \end{bmatrix} \tag{3.3}$$

The minimization of the energy function defined in equation 3.1 can then be achieved by solving the following system of equations

$$L_U x_U^s = -B f^s \tag{3.4}$$

where f^s is a $|V_M|$x1 indicator vector for the labeled vertices that defines the segmentation boundary.

$$f_j^s = \begin{cases} 1 & \text{if } y_j = s \\ 0 & \text{if } y_j \neq s \end{cases} \tag{3.5}$$

where $y_j = \max_s v_j^s$.

3.3.2 Incorporating Prior Models

Without incorporating prior models, the random walker formulation fails to segment disconnected objects since, each segment must be connected to a seed. To remedy this problem,

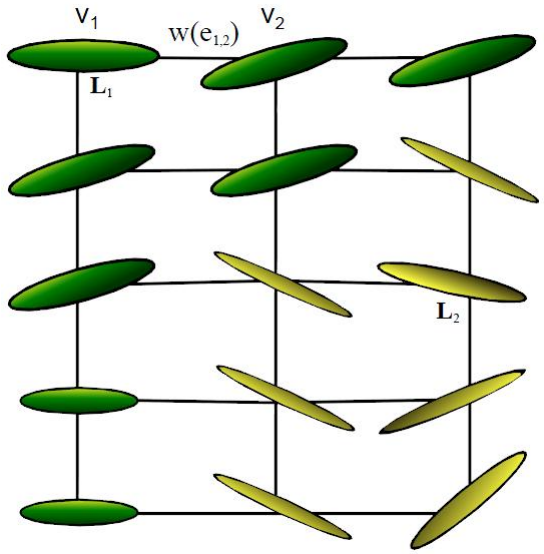

(a) Graph with seed points

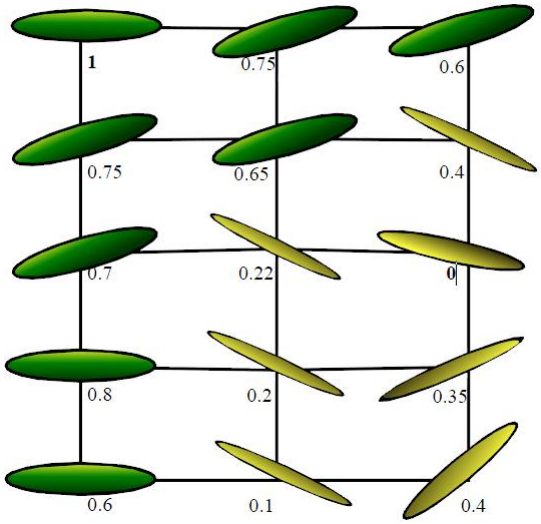

(b) Probability that a random walker starting from each node first reaches seed L_1

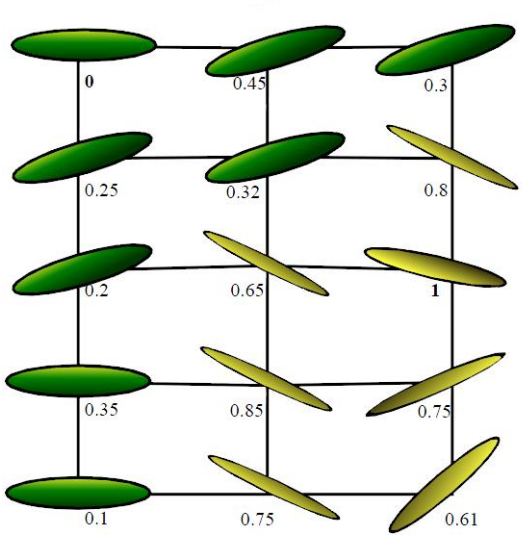

(c) Probability that a random walker starting from each node first reaches seed L_2

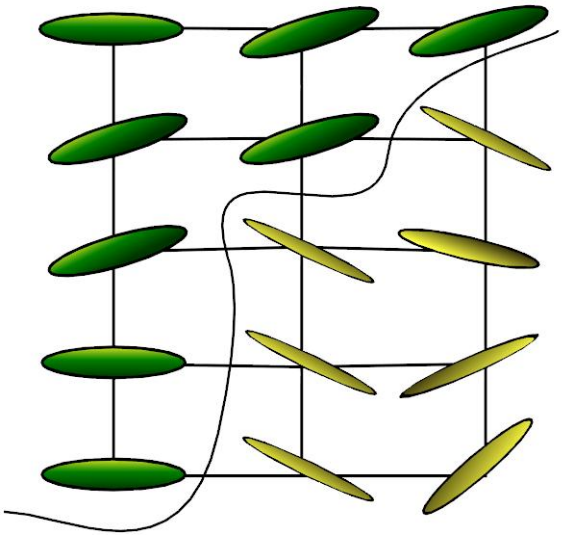

(d) Segmentation result

Figure 3.1: Illustration of the approach to segmentation with two seed points representing two labels (L_1, L_2). (a) shows the initial seed points where each node is a diffusion tensor. Ellipsoids are used to visualize the diffusion tensors where the directions and lengths of the major axes correspond to the eigenvectors and eigenvalues of the diffusion tensors. (b),(c) show the probabilities that a random walker starting from each node first reaches a seed. (d) shows the expected segmentation result.

the probability P_i^s that each node v_i belongs to each label s based on the label's tensor distribution is calculated. From the user initialized seed regions, a tensor distribution can be estimated using a kernel density estimation. So that, for each tensor a nodewise prior (P_i^s) is calculated. The prior P_i^s represents the probability that the tensor at vertex v_i belongs to the tensor distribution of label s. Each label is assumed to be equally likely, therefore using Baye's theorem the probability that a node v_i belongs to a label s is given as [17]

$$x_i^s = \frac{P_i^s}{\sum_{s=1}^{k} P_i^s} \tag{3.6}$$

The equation above can be rearranged to solve for the nodewise priors (in vector notation)

$$\left(\sum_{s=1}^{k} \Lambda^s\right) x^s = P^s \tag{3.7}$$

where Λ^s is a diagonal matrix with the values of P^s on its diagonal. This leads to the introduction of the priors into the system of equations given in 3.1 which are used to find the probabilities x_U^s . The new system of equations can be defined as

$$\left(L_U + \gamma \sum_{r=1}^{k} diag\left(P_U^r\right)\right) x_U^s = \gamma P_U^s - B f^s \tag{3.8}$$

where γ is a free parameter. The aim is to solve for the unknown probabilities (x_U^s). Using Matlab the system of equations can be solved using the backslash command (\).

$$x_U^s = \left(L_U + \gamma \sum_{r=1}^{k} diag\left(P_U^r\right)\right) \backslash \gamma P_U^s - B f^s \tag{3.9}$$

A Gaussian kernel is used to produce the probability density estimation of the tensors in each user supplied label. Given a set of n labeled tensors (seeds) $R^s = \{R_1^s, R_2^s, ..., R_n^s\}$ for each user defined label s, the probability P_i^s that a tensor T_i is generated from the seeds distribution corresponding to label s is given by

$$P_i^s = \sum_{q=1}^{n} exp\left(\frac{\left(\mathrm{d}\left(T_i, R_q\right)\right)^2}{\sigma^2}\right) \tag{3.10}$$

where $\mathrm{d}(T_i, R_q)$ is the tensor distance between a pair of tensors T_i and R_q, σ is a free parameter.

3.3.3 Tensor Distance Metrics

The weights on the edges between the verticies on the graph represent how similar or dissimilar two vertices are. When dealing with scalar images, the intensity difference of two vertices (pixels) is sufficient to indicate the similarity between the two verticies. However, when dealing with diffusion tensors appropriate tensor distances have to be used. A proper distance metric should incorporate both diffusion magnitudes (eigenvalues) and directions (eigenvectors) in the DT-MR image.

The simplest and most straight forward distance between two tensors T_1,T_2 can be calculated using a Euclidean metric. This distance is given by the "Frobenious distance" which is simply

$$d_F = \text{Trace}\,(T_1 - T_2)^2 \tag{3.11}$$

Euclidean distances tend to be unsatisfactory for tensors, since they allow the presence of null or negative eigenvalues, which is physically infeasible and doesn't make sense for diffusion tensors. The second problem with taking the Euclidean difference, is that the euclidean averaging of tensors can lead to a tensor swelling effect because the determinant of the Euclidean mean can be larger than the determinant of the original matrices, which introduces more dispersion to the computations and hence, more diffusion which is an unwanted effect. The third and last issue, also involves the Euclidean mean. The Euclidean mean, is an arithmetic mean which fails to represent the tensor's identity or inverse. The geometric mean is a better choice when modeling tensor variability.

The Log-Euclidean[5] and J-divergence[31] are both affine invariant tensor distance measures that take advantage of both diffusion magnitude and direction, which makes them a good choice for finding the edge weights of the constructed graph for the segmentation. With affine invariant metrics, symmetric matrices with negative or null eigenvalues are at an infinite distance from any tensor and there is no swelling effect.

The Log-Euclidean tensor distance D_{LE} performs classical Euclidean calculations in the domain of matrix logarithms. A tensor T_i has a unique symmetric matrix logarithm $L_T = \log(T_i)$, where L_T can be calculated in three steps:

1. Diagonalize T_i to obtain two matrices. A rotation matrix $\mathbf{R}$ (eigenvectors) and a diagonal matrix $\mathbf{E}$ with the eigenvalues on it's diagonal.

2. Take the natural logarithm of each diagonal element in $\mathbf{E}$ to obtain a new matrix $\tilde{E}$

3. Recompose $\tilde{E}$ and $\mathbf{R}$ to obtain the logarithm of the tensor. $log\left(T_i\right) = R^T \cdot \tilde{E} \cdot R$

The Log Euclidean tensor distance satisfies several invariance properties. For instance, distances are unaffected by inversion. Since, the inversion of system of matrices results in the multiplication of -1 of their logarithms. This does not change the value of the distance. Moreover they are invariant to logarithmic multiplication which makes them invariant to translation. The Log Euclidean distance metric is given by [5]

$$d_{LE}\left(T_i, T_j\right) = \sqrt{\text{Trace}\left(\left(log\left(T_i\right) - log\left(T_j\right)\right)^2\right)} \tag{3.12}$$

On the other hand, the J-divergence d_{JD} uses the distance measure between Gaussian distributions to find the distance between tensors. Since, the direction of water diffusion can be locally modeled by a Gaussian probability density function. A diffusion tensor $\mathbf{D}$ is related to the displacement $\mathbf{r}$ of water molecules at each lattice point in an image at time t by

$$p\left(r|t, D\right) = \frac{1}{\sqrt{\left(2\pi\right)^n \left|2tD\right|}} e^{\frac{-r^T D^{-1} r}{4t}} \tag{3.13}$$

where n is the tensor's dimension. Therefore, one can find the distance between two tensors using a Gaussian distribution distance measure. The Kullback-Leibler (KL) divergence is the most widely used measure for Gaussian distributions

$$KL\left(p||q\right) = \int p\left(x\right) log \frac{p\left(x\right)}{q\left(x\right)} dx \tag{3.14}$$

However, the KL divergence is not symmetric, therefore the J-divergence is used to make it symmetric. The proposed J-divergence tensor distance is the square root of the J-divergence [31]

$$d_{JD}\left(T_i, T_j\right) = \sqrt{tr\left(T_i^{-1} T_j + T_j^{-1} T_i - 2I\right)} \tag{3.15}$$

where I is a 3x3 identity matrix.

3.3.4 Calculating the Weights

For scalar images the following equation is used for mapping vertex intensities (I_i, I_j) to connecting weights

$$w_{ij} = e^{-\beta\left(I_i - I_j\right)^2} + \epsilon \tag{3.16}$$

The equation is modified to find the weights between tensors

$$w_{ij} = e^{-\beta \text{ d } \left(T_i, T_j\right)^2} + \epsilon \tag{3.17}$$

where ϵ is a small constant, and β is a free scaling parameter. $\mathrm{d}(T_i, T_j)$ is the distance between two tensors T_i, T_j. Both the Log Euclidean (d_{LE}) and J-divergence distance (d_{JD}) metrics are used to calculate two different sets of weights. The tensor distances (d_{LE} and d_{JD}) are normalized to a range of [0,1].

3.4 Results

Various segmentations were performed using the above technique. Segmentation results using both tensor distance metrics (Log Euclidean and J-divergence) are presented for comparison purposes. Moreover, the advantage of incorporating prior models is demonstrated.

For our experiments the β parameter in equation 3.17 had a significant effect on the results of the segmentations. A different value had to be used for the two different tensor distance metrics to achieve a similar segmentation result. This is expected since both measures have a different scale and return different values for the same graph.

The β parameter also had an effect on the quality and the smoothness of the segmentation result. The optimal β parameter in our experiments was determined by trial and error. Multiple values were tested until a qualitatively satisfactory segmentation was achieved. The other free parameter σ in equation 3.10 was also determined the same way, and it also had an effect on the quality of the segmentation.

Standard hard constraints were used in all the examples. Both background and object seeds were provided as user input. For all the segmentation results, the object seeds are shown in green and the background seeds in yellow.

The segmentations are performed on selected slices from the DT-MRI data sets using all the information provided by the tensors. The slices are visualized by taking the trace which are painted with seeds by the user. The location of the seeds is then extracted from the scalar images and are used in the random walker segmentation method. Note that the segmentation is carried on the DT-MRI data set and not on the scalar images used to visualize the segmentation results. Performing segmentations on the scalar images would produce comparable results, however the advantage of using all the information provided by the tensors is lost. Especially that scalar metrics only take into account a tensor's eigenvalues and don't take the eigenvectors into consideration.

3.4.1 Synthetic Data Sets

The first experiment is that of an object made of several disconnected parts in Fig 3.2. The data set is a synthetic noisy DT-MRI slice containing an object with several disconnected parts. Noise was added to the data set by adding random Gaussian noise independently to the three eigenvalues of the DT-MR image, in addition to random rotation perturbing the three eigenvectors by the same amount to retain orthogonality. Segmenting the image without the incorporation of prior models fails to detect all three disconnected objects. Only the object that was seeded was the result of the segmentation. Fig 3.2 additionally shows the effect of changing the β parameter on the result of the segmentation. Using the same β parameter for both Log Euclidean and J-Divergence metrics lead to different segmentation results.

Fig 3.3 shows the same data set used in Fig 3.2. However, the segmentation result was reached by incorporating the prior models. Again, only one of the disconnected objects was seeded. However, all three disconnected objects are detected and make up the result of the segmentation. Also, less seeds were needed as an input to obtain a correct segmentation. Only the Log Euclidean distance metric was used for the segmentations with prior models.

In Fig 3.4, the synthetic data set is constructed in a way to demonstrate that full tensor information is needed for DT-MRI segmentation techniques. The data set contains two different tensor fields with the same magnitude (eigenvalues) but pointing in two different directions (eigenvectors).The inner dark disk contains tensor pixels with eigenvectors (1, 0, 0), (0, 1, 0), (0, 0, 1) and eigenvalues of (10, 1, 1). The outer disk contains tensors with eigenvectors (0, 1, 0), (1, 0, 0), (0, 0, 1) and eigenvalues of (10, 1, 1). Gaussian noise was added independently to the three eigenvalues of the DT-MR image. A segmentation algorithm that only takes the tensors magnitude into account would fail to produce a proper segmentation. However, since our proposed technique takes into account both diffusion direction and magnitude the result of the segmentation was accurate and as expected.

3.4.2 Real Data Sets

The proposed segmentation technique was also tested on real medical data sets. Fig 3.5, shows the application of the segmentation technique on a brain data set. The brain DT-MRI

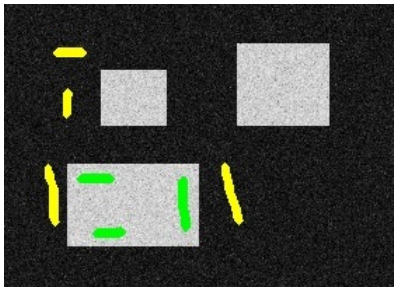

(a) Initial image with foreground seeds placed only in the lower rectangle

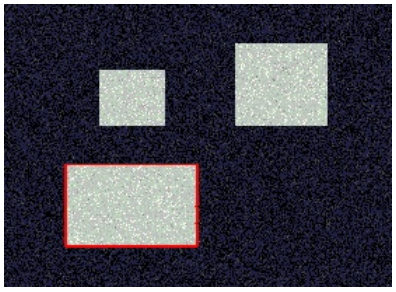

(b) Segmentation using the Log Euclidean metric leads to the correct segmentation of the lower rectangle ($\beta = 40$)

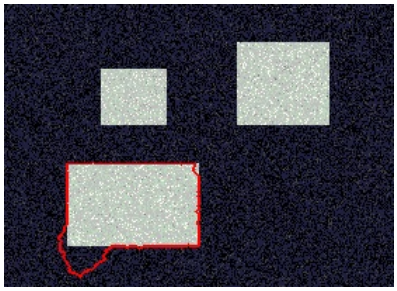

(c) Segmentation using the J-Divergence metric with a β=40 leads to an incorrect segmentation result

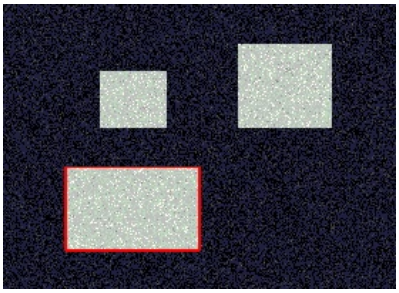

(d) Segmentation using the J-Divergence metric with a different β value (β=790) leads to a correct segmentation of the lower rectangle

Figure 3.2: Segmentation of a noisy synthetic 2D DT-MRI slice which contains disconnected objects without priors. Demonstrating the effect of the β parameter on the segmentation result.

data set was provided by Dr. Mirza Faisal Beg, School of Engineering Science at Simon Fraser University. In this experiment the corpus callosum is segmented from the remaining parts of the brain. The corpus callosum area in the brain constitutes of white matter which is highly anisotropic compared to the surrounding isotropic gray matter.

Fig 3.6 shows the segmentation result of a cardiac wall from a DT-MRI slice of the heart. The data set is publicly available by the Center for Cardiovascular Bioinformatics and Modeling at The John Hopkins University (http://www.ccbm.jhu.edu/research/DTMRIDS.php). Without using prior models, the random walker segmentation technique failed to segment the cardiac wall accurately. A more satisfactory segmentation without using prior models

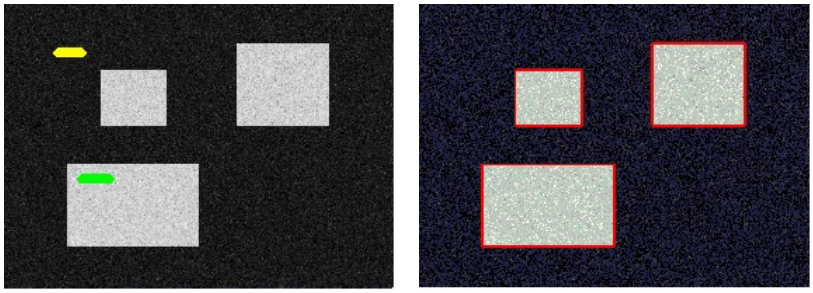

(a) Initial image with seeds

(b) Segmentation using the Log Euclidean metric ($\beta = 90$, $\sigma = 4$)

Figure 3.3: Segmentation of a noisy synthetic 2D DT-MRI slice which contains disconnected objects with the incorporation of priors. All three rectangles are identified and segmented from the background.

for this data set was achieved by increasing the number of supplied seeds as displayed in Fig 3.7. However, when prior models were incorporated a satisfactory and expected segmentation was achieved as shown in Fig 3.8. This demonstrates that using prior models can also be of an advantage when dealing with noisy data sets. Fig 3.7 shows that even with the increased number of supplied hard constraints (seeds), the segmentation result isn't as accurate as the one produced when the prior models are used.

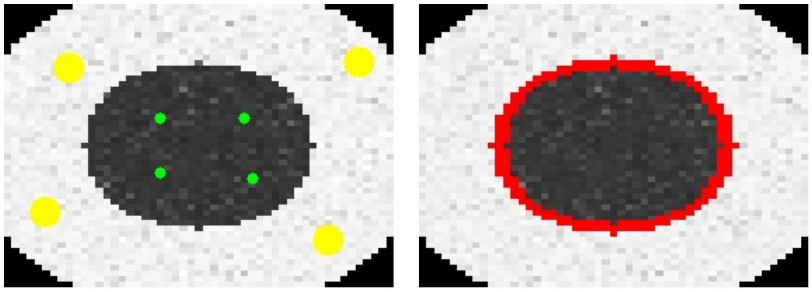

(a) Initial image with seeds

(b) Segmentation result using the Log Euclidean metric ($\beta = 19$)

Figure 3.4: Segmentation of a noisy synthetic 2D DT-MRI slice. The inner seeded disk is correctly segmented from the noisy background.

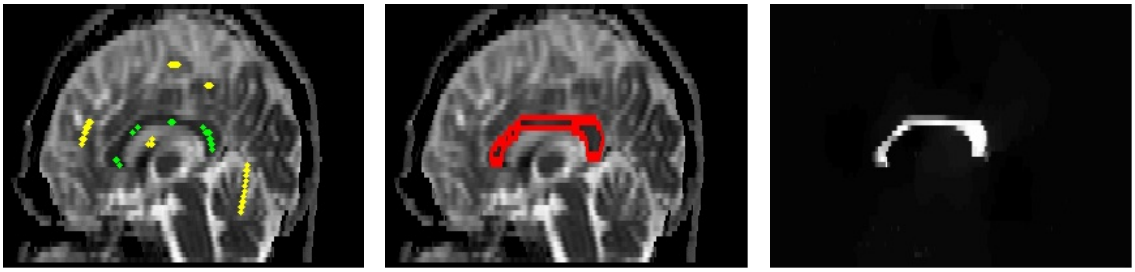

(a) Initial image with seeds

(b) segmentation result using the Log Euclidean metric ($\beta = 50$)

(c) the shape of the segmented corpus callosum

Figure 3.5: Segmentation of the corpus callosum from a real brain DT-MRI dataset.

The segmentation result of the white matter from a DT-MRI slice of the brain is shown in Fig 3.9. This example shows the advantage of using prior models for brain segmentation. The user only needs to supply one set of seeds to completely segment the white matter in the brain. To achieve a similar segmentation result without using prior models the user would have to supply many more seeds and manually select multiple areas where the white matter is present.

3.4.3 A Comparison between Random Walker and Graph Cuts

To demonstrate the differences between applying different segmentation methods on DT-MRI data, we compare segmentation results obtained by using the random walker and

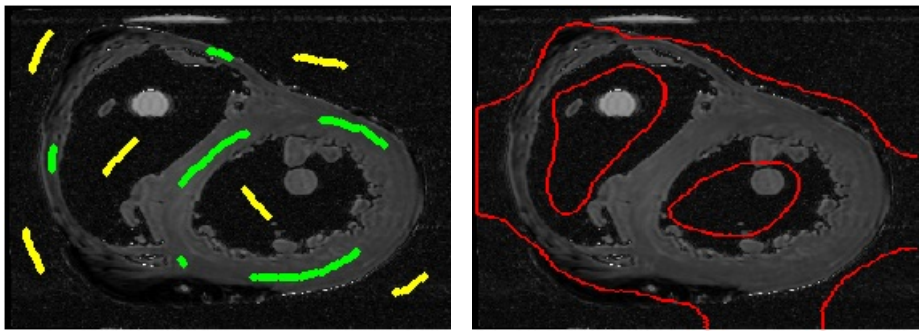

(a) Initial image with seeds

(b) Segmentation result without prior models (β=40)

Figure 3.6: Cardiac wall segmentation from a DT-MRI slice of the heart with no prior models.

graph cuts segmentation methods. Segmentation results obtained by applying the random walker method are qualitatively compared to segmentation results obtained on the same set of images using the graph cuts segmentation method. For the random walker results the segmentation result is displayed as a red outline, whereas the graph cuts segmentation results are shaded in green. As before, foreground seeds are shown in green and background seeds on the initial images are shown in yellow. Both the random walker and graph cuts approaches in this implementation incorporate the user initialized seeds as hard constraints. The graph cuts approach also has a free parameter (λ) that affects the segmentation results.

Fig 3.10 shows the results of applying both segmentation methods on a DT-MRI slice of the heart. The random walker segmentation method (Fig. 3.10(b)) returned a much accurate result than the application of the graph cuts segmentation method (Fig. 3.10(c)). The result returned using the graph cuts leaked outside of the heart region and included the noise present at the top edge of the DT-MRI slice.

Fig 3.11 shows the result of the segmentation of the corpus callosum from a DT-MRI slice of the brain. No prior models were incorporated in the random walker formulation to obtain the result. The random walker returned a more accurate result than the graph cuts. Again, the graph cuts result included areas which should not be part of the segmentation.

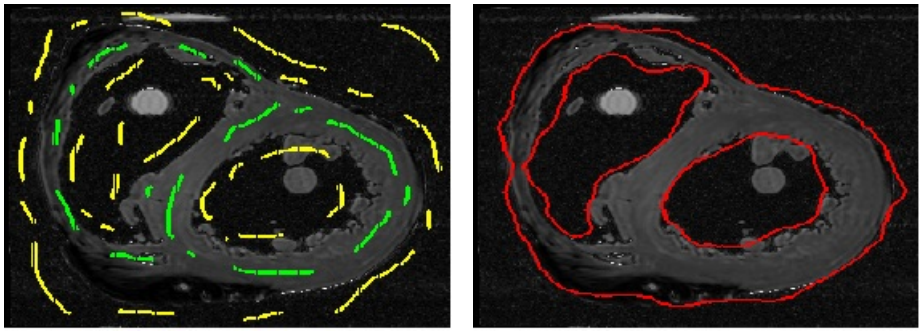

(a) Initial image with seeds

(b) Segmentation result without prior models (β=40)

Figure 3.7: Cardiac wall segmentation from a DT-MRI slice of the heart with additional seeds and no prior models.

3.5 Discussion

The random walker segmentation technique has previously only been applied to scalar images. We have shown in this work that the random walker segmentation algorithm can be extended to segment DT-MR images. Moreover, prior models were incorporated into the energy minimization function. The incorporation of prior models overcomes the problems associated with the original formulation of the random walker technique. For instance, without using prior models the algorithm fails to segment images that contain disjoint objects. This means that the user would have to seed each disjoint object individually which can be time consuming and unpractical.

A Gaussian kernel was used to produce the densities corresponding to each of the user supplied K labels. Moreover, tensor dissimilarity metrics were used to define the edge weights and to compute the prior models. More specifically, both the Log euclidean and J-divergence metrics were used. Both distance metrics lead to accurate and intuitive segmentations. The only difference is that the β parameter in equation 3.17 had to be set differently for both distance metrics for the same image. The fact that the two different distance metrics gave similar segmentation results is no surprise since both metrics provide two different generalizations to tensors of the geometric mean of positive numbers. The determinants of both Log-Euclidean and J-divergence means of tensors are equal to the scalar geometric mean of the determinants of the data.

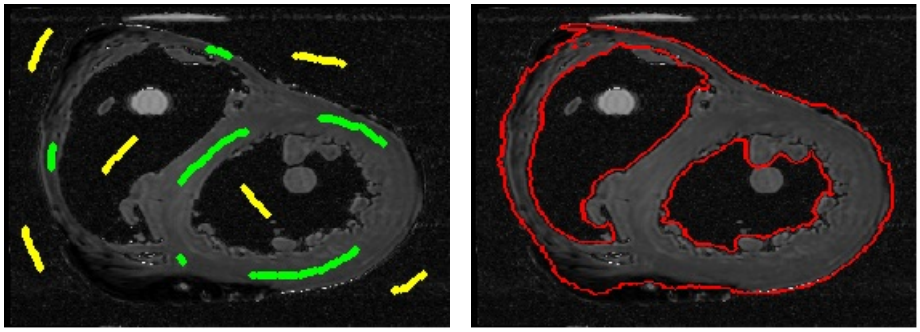

(a) Initial image with seeds

(b) Segmentation result with prior models (β = 700, σ =10)

Figure 3.8: Cardiac wall segmentation from a DT-MRI slice of the heart with prior models.

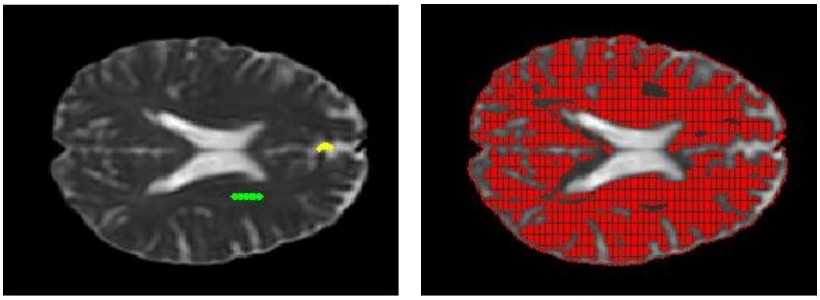

(a) Initial image with seeds

(b) Segmentation result with prior models (β = 100,σ = 1)

Figure 3.9: White matter segmentation from a DT-MRI slice of the brain.

The proposed approach was tested on both real and synthetic DT-MR images. The synthetic images have Gaussian noise added to them, to demonstrate the robustness of the algorithm. Qualitatively, the segmentation results appear accurate and satisfactory. The advantages of using the random walker with prior models is demonstrated in several examples. Using prior models lead to better results when disjoint objects are present and also when the data sets are very noisy. Our segmentation results were very sensitive to the free beta parameter that is used in equation 3.17 to calculate the weights of the graph's edges. Also, the two tensor distance metrics give different segmentation results for the same parameter values. Future work will investigate how to select a suitable value for β and the

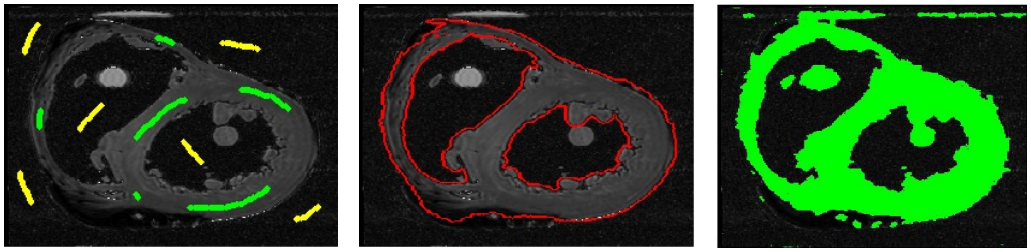

(a) Initial image with seeds (b) Segmentation using Random walker ($\beta = 700$, $\sigma = 10$) (c) Segmentation using Graph cuts ($\lambda = 900$)

Figure 3.10: Comparison of the cardiac wall segmentation from a DT-MRI slice of the heart

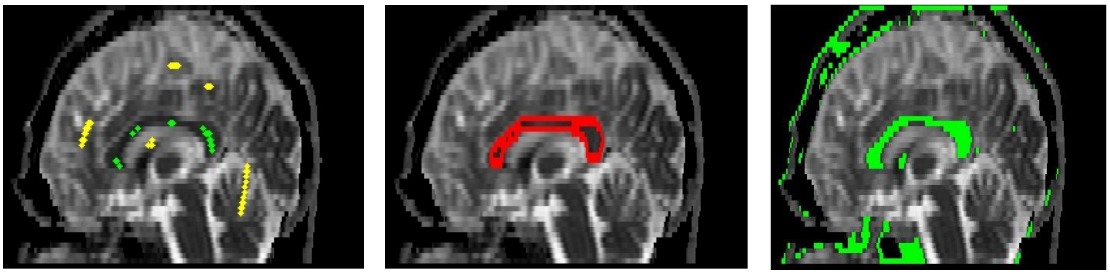

(a) Initial image with seeds (b) Segmentation using Random walker ($\beta = 50$) (c) Segmentation using Graph cuts ($\lambda = 5$)

Figure 3.11: Segmentation of the corpus callosum from a DT-MRI slice of the brain.

validation of the segmentation results using quantitative measures.The segmentation results were also compared to those produced by applying the graph cuts segmentation method. The random walker returned more accurate segmentations than the graph cuts on all the data sets it was tested on.

Chapter 4

4^{th} Order Versus 2^{nd} Order DT-MRI Segmentations

4.1 Introduction

In DT-MRI processing, a 2^{nd} order tensor has been commonly used to approximate the diffusivity function at each voxel in a DT-MRI dataset. This tensor approximation can be used to calculate scalar quantities such as Fractional Anisotropy. Such scalar measures are used for monitoring many neurological disorders such as encephalopathy, sclerosis and ischemia.

The scalar measures are computed using the 2^{nd} order diffusion tensor, which is sufficient for simple tissue structures. However, it fails to approximate more complex tissue geometry with multi lobed diffusivity profiles. This is demonstrated by the drop in FA values in areas of fiber crossings although these areas are anisotropic [6].

The 2^{nd} order tensor models fail to correctly represent complex tissue structures because 2^{nd} order tensors possess only a single orientational direction (the major eigenvalue of the diffusion tensor). It is important to be able to represent such areas correctly since, the cerebral white matter contains considerable areas that demonstrate intravoxel orientational heterogeneity (IVOH). Given the widespread divergence and convergence of fascicles and fiber tracts in white matter.

Diffusion tensors can be visualized as ellipsoids, where the radius defines the diffusion in a particular direction. Since, 2^{nd} order diffusion tensors are only capable of representing

one direction the ellipsoid resulting from areas of crossing fibers is oblate (pancake-shaped) i.e. a diffusion tensor in which the first eigenvalue is comparable to the second and both are much larger than the third. This can be explained using the analogy of adding two rank 1 tensors with different directions (Fig 4.1). The result of the addition is a rank 2 tensor [34]. The resulting tensor has more degrees of freedom than the input tensors and can only describe the plane in which the diffusion is present.

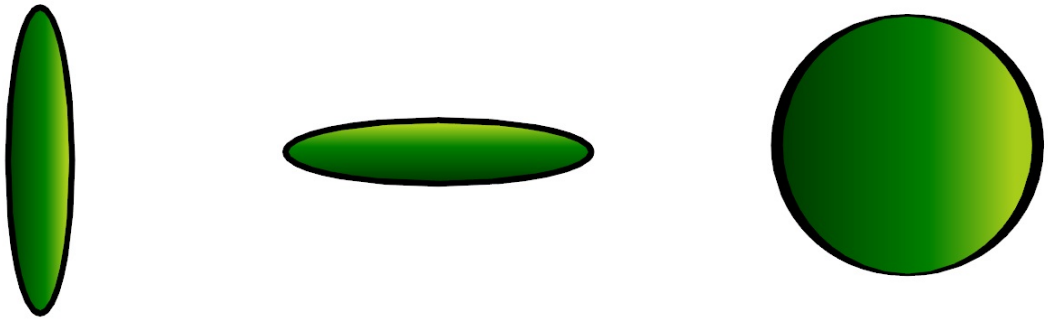

(a) (b) (c)

Figure 4.1: Two diffusion tensors of rank 1 and their summation which gives a rank 2 tensor. The tensors are visualized as ellipsoids with the eigenvectors forming the principle axes.

Several approaches have been proposed to overcome the limitation of 2^{nd} order tensors. Tuch et al.[30] proposed a method that uses diffusion imaging with diffusion-weighting gradients supplied along many directions, distributed isotropically on the surface of a unit sphere. This method is called high angular resolution diffusion imaging (HARDI). The method uses high angular resolution, high b-value diffusion gradient sampling. The high b-values are used to enhance the contrast between the fast diffusion component of one fiber and the slow diffusion component of another. The diffusion imaging is performed with diffusion weighted gradients along many directions that are distributed isotropically on the surface of a unit sphere. Multiple fiber components are identified by calculating the probability distribution function (PDF) of the diffusion process in each voxel. However, this method is time and computationally intensive and therefore, is impractical for clinical use.

Frank [16] introduced an improvement to the HARDI method that provides the ability to transform the distribution of diffusivities into components of a higher order tensor. This is accomplished by calculating the spherical harmonic transform of the diffusivity profile

and the resulting Laplace series is truncated. However, the truncation is not consistent with Stejskal's modification for anisotropic media.

Ozarslan et al.[26] propose a method that provides a Cartesian representation of higher order diffusion tensors. The method resolves the problem with the process of calculating the spherical harmonic transform of the diffusivity profile and the truncation of the Laplace series. The expression resulting from the method corresponds to the Stejskal-Tanner relation which allows for the calculation of all the components of a higher-rank diffusion tensor by using a least-squares fitting routine. Therefore, the evaluation of the spherical harmonic transform is unnecessary, which is computationally intensive. The higher order tensors have the ability to generalize the 2^{nd} order tensors and can represent more complex tissue geometry with multi-lobe diffusivity profiles. This approach is especially attractive because the algorithms and metrics developed for 2^{nd} order tensors can be extended to higher order tensors.

A general order-k Cartesian tensor has 3^k terms, which results in a large number for higher order tensors. A 4^{th} order tensor has 81 components whereas a 2^{nd} order tensor only has 9. However, symmetries provide a significant reduction in the number of the tensor's components. The diffusion tensor's total symmetry property reduces the number of distinct elements (N_k) to [7]

$$N_k = \frac{(k+1)(k+2)}{2} \tag{4.1}$$

which means that a 4^{th} order tensor has 15 unique elements.

4.2 Contribution

In this chapter, we extend the random walker segmentation algorithm proposed for the segmentation of scalar images to segment both 2^{nd} and 4^{th} order DT-MR image data, published in[14]. The DT-MRI data is converted to a graph where each tensor is a vertex and is connected to neighboring tensors by a weighted edge. The edges are evaluated using appropriate distance metrics that quantify the similarity between two tensors. The metric used for 2^{nd} order tensors is the Log-Euclidean [5] whereas the L_2 distance [6] is used for the 4^{th} order tensors.The advantages of performing segmentation on higher order data is demonstrated.

Section 4.3.1 presents the tensor distance metrics used, section 4.3.2 explains how the

weights on the graph are calculated. The experimental segmentation results on both synthetic and real DT-MRI data is presented in section 4.4. Concluding remarks are made in section 4.5.

4.3 Methods

Please refer to Chapter 3 section 3.1 for a review of the random walker segmentation method and section 3.2 for details on the 2^{nd} order distance metric used in the method presented here.

4.3.1 Tensor Distance Metrics

The edge weights of the constructed graph represent how similar or dissimilar two vertices are. When dealing with diffusion tensors appropriate tensor distance metrics have to be used. More specifically, the metrics should utilize all the information provided by the tensors. So both the diffusion magnitude (eigenvalues) and direction (eigenvectors) should be incorporated.

The Log-Euclidean tensor distance (d_{LE}) performs Euclidean calculations in the domain of matrix logarithms and can be used to find the distance between two 2^{nd} order tensors (T_i, T_j) [5]

$$d_{LE}\left(T_i, T_j\right) = \sqrt{\text{Trace}\left(\left(log\left(T_i\right) - log\left(T_j\right)\right)^2\right)} \tag{4.2}$$

On the other hand, a distance measure between 4^{th} order diffusion tensors (D_i, D_j) can be computed using the normalized L_2 norm between the corresponding diffusivity functions $d_1\left(g\right)$ and $d_2\left(g\right)$. The diffusivity function is first represented using a 4^{th} order tensor as [6]:

$$d\left(g\right) = \sum_{i+j+k=4} D_{i,j,k} g_1^i g_2^j g_3^k \tag{4.3}$$

where $g = [g_1,\ g_2,\ g_3]^T$ is the magnetic field gradient direction. Diffusion is symmetric therefore, the 4^{th} order model results in voxels that are $3 \times 3 \times 3 \times 3$. The diffusion tensors are totally symmetric positive definite matrix with 15 unique coefficients; whereas the 2^{nd} order model results in a 3×3 symmetric positive definite matrix with 6 unique coefficients.

The normalized L_2 distance between two 4^{th} order diffusivity functions is computed using the following equation [6]

$$
\begin{aligned}
d_{L2}^2\left(D_1, D_2\right) &= \frac{1}{4\pi}\int_{s^2}\left[d_1\left(g\right) - d_2\left(g\right)\right]^2 dg \qquad (4.4)\\
&= \frac{1}{315}[\left(\Delta_{4,0,0} + \Delta_{0,4,0} + \Delta_{0,0,4} + \Delta_{2,2,0} + \Delta_{0,2,2} + \Delta_{2,0,2}\right)^2\\
&+4[\left(\Delta_{4,0,0} + \Delta_{2,2,0}\right)^2 + \left(\Delta_{4,0,0} + \Delta_{2,0,2}\right)^2 + \left(\Delta_{4,0,0} + \Delta_{2,2,0}\right)^2\\
&+\left(\Delta_{0,4,0} + \Delta_{0,2,2}\right)^2 + \left(\Delta_{0,0,4} + \Delta_{0,2,2}\right)^2 + \left(\Delta_{0,0,4} + \Delta_{2,0,2}\right)^2]\\
&+24\left(\Delta_{4,0,0}^2 + \Delta_{0,4,0}^2 + \Delta_{0,0,4}^2\right) - 6\left(\Delta_{2,2,0}^2 + \Delta_{0,2,2}^2 + \Delta_{2,0,2}^2\right)\\
&+2\left(\Delta_{4,0,0} + \Delta_{0,4,0} + \Delta_{0,0,4}\right)^2 + \left(\Delta_{2,1,1} + \Delta_{0,3,1} + \Delta_{0,1,3}\right)^2\\
&+\left(\Delta_{1,2,1} + \Delta_{3,0,1} + \Delta_{1,0,3}\right)^2 + \left(\Delta_{1,1,2} + \Delta_{3,1,0} + \Delta_{1,3,0}\right)^2\\
&+2[\left(\Delta_{3,1,0} + \Delta_{1,3,0}\right)^2 + \left(\Delta_{3,0,1} + \Delta_{1,0,3}\right)^2 + \left(\Delta_{0,3,1} + \Delta_{0,1,3}\right)^2]\\
&+2\left(\Delta_{3,1,0}^2 + \Delta_{3,0,1}^2 + \Delta_{1,3,0}^2 + \Delta_{0,3,1}^2 + \Delta_{1,0,3}^2 + \Delta_{0,1,3}^2\right)] \qquad (4.5)
\end{aligned}
$$

where the integral is over all unit vectors and the coefficients $\Delta_{i,j,k}$ are computed by subtracting the coefficients $D_{i,j,k}$ of the tensor D_i from the corresponding coefficients of the tensor D_j. In this work, we denote the coefficients of the 4^{th} order diffusion tensor using the notation used in [6], i.e., $D_{i,j,k}$, where $i + j + k = 4$. For example, $D_{4,0,0}$ refers to D_{xxxx}. The integral in equation 4.4 can be computed analytically and the result can be expressed as a sum of squares of the terms $\Delta_{i,j,k}$ as shown in equation 4.5. This makes the implementation of the distance measure between 4^{th} order tensors efficient. Note that the distance measure is invariant to rotations since the integral is defined over all gradient directions.

4.3.2 Calculating the Weights

Using the distance metrics the edge weights on the graph can be calculated using the following equation,

$$w_{ij} = e^{-\beta d\left(T_i, T_j\right)^2} + \epsilon \qquad (4.6)$$

where ϵ is a small constant and β is a free scaling parameter set by the user. d is $d_{LE}\left(T_i, T_j\right)$ when performing segmentation on 2^{nd} order tensors and $d_{L2}\left(D_i, D_j\right)$ when performing segmentation on 4^{th} order tensors. The tensor distances are normalized to a range of [0,1].

4.4 Results

Segmentations were performed on both 2^{nd} and 4^{th} order DT-MR images using the above methodology. Positive definite tensors of 2^{nd} and 4^{th} order were estimated using the method proposed by Barmpoutis et al. [6]. Segmentation results of both 2^{nd} and 4^{th} order datasets are presented for comparison purposes. The advantage of performing segmentation on 4^{th} order datasets instead of 2^{nd} order is demonstrated.

Standard hard constraints were used in all the examples. Both background and object seeds were provided as an input. For all the segmentation results, the object seeds are shown in green and the background seeds in yellow. Moreover, the DT-MR images sets are visualized using the trace. For our experiments the β parameter in equation 4.6 had a noticeable effect on the results of the segmentations. The optimal β parameter in our experiments was determined by trial and error. Multiple values were tested until a qualitatively satisfactory segmentation was achieved.

4.4.1 Synthetic Data Sets

Our synthetic dataset presented here is of size 100x100 and contains a 40x40 box which is composed of simulated crossing fibers with orientations of [0.7071 0.7071 0] and [0.7071 -0.7071 0]. The box is surrounded by simulated crossing fibers with orientations of [1 0 0] and [0 1 0]. Fig. 4.2 shows both the 2^{nd} and 4^{th} order diffusion tensor fields reconstructed from the same synthetic image slice and are visualized via a spherical visualization technique [1]. The 2^{nd} order approximation did recognize that the two types of crossing fibers are different (demonstrated by the difference in color in the visualization) however, the approximation shows all the tensors as being planar and no crossing is depicted. It fails to distinguish the inner box from the surrounding fibers. Whereas, the 4^{th} order approximation can differentiate between both regions and correctly displays the crossing fibers. Note that to avoid tensor cluttering, we plot the tensors at intervals of 10.

Fig. 4.3 shows the segmentation result of the synthetic dataset, where the aim is to segment the middle black box from the white background. The segmented result is shown by the red outline. Fig. 4.3(b) clearly shows that the 2^{nd} order model fails to segment the middle box because the 2^{nd} order tensor model lacks the ability to distinguish between

[1] The visualization is performed using a computer program implemented by Barmpoutis and is available at: http://www.cise.ufl.edu/ abarmpou/lab/

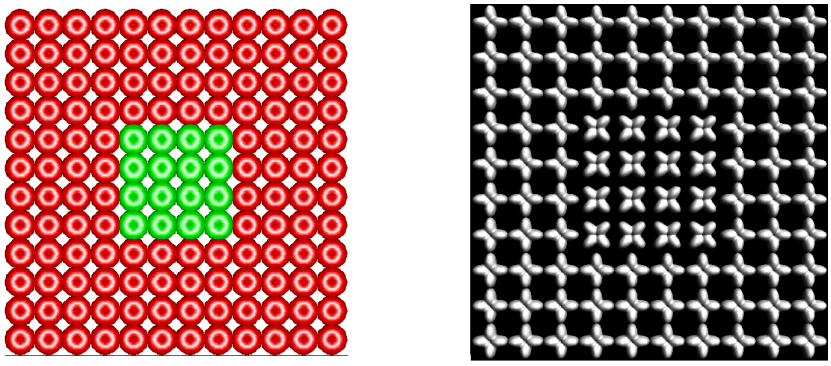

(a) 2^{nd} order tensors (b) 4^{th} order tensors

Figure 4.2: Spherical visualization of the synthetic data set.

crossing fibers, whereas the 4^{th} order model accurately segments the middle box as shown in fig. 4.3(c). This also serves to demonstrate that the normalized L_2 distance metric takes into account both the direction and the magnitude of the 4^{th} order diffusion tensors.

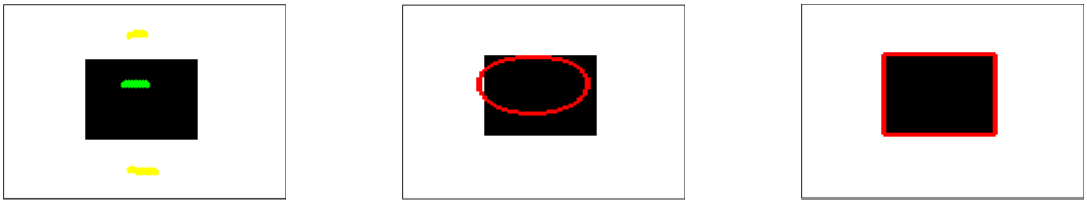

(a) Initial image with seeds (b) 2^{nd} order tensors segmentation (c) 4^{th} order tensors segmentation

Figure 4.3: Segmentation result of the synthetic data set.

4.4.2 Real Data Sets

The proposed segmentation technique was also tested on a real medical data set. We would like to acknowledge Jennifer Campbell of the McConnell Brain Imaging Centre, Montreal

Neurological Institute, McGill University for the fourth order data set. The dataset presented here consists of a human brain where 99 Diffusion Weighted (DW) volumes are acquired in 99 gradient directions.There is one S_0 volume acquired with no gradient direction and the B-value is 3000.

Region of interest to segment

Fig. 4.4 describes the region of interest chosen to demonstrate the advantage of using fourth order tensors for the segmentation of DT-MRI data. A region where fiber tracts are present is chosen as an area of interest to demonstrate that using a fourth order dataset results in a better segmentation result. Note that the second order dataset is reconstructed from the fourth order dataset using Barmpoutis and Vemuri's method presented in [1]. The trace of the second and fourth order slice is calculated to visualize the selected slice. This is to confirm that the same slice is selected from both the 2^{nd} and 4^{th} data sets. The top right corner of the slice is selected as a region of interest because of the presence of white fiber tracts. The selected region of interest is shown on both the trace of the 2^{nd} (fig. 4.4(a)) and 4^{th} (fig. 4.4(b)) order slices. To visualize the fibers and demonstrate their presence in the selected area, the Fractional Anisotropy (FA) is calculated for the second order slice (fig. 4.4(c)) whereas the Generalized Anisotropy (GA) is calculated for the fourth order slice (fig. 4.4(d)).

Fig. 4.5 shows the segmentation result of the fibers performed on both the 2^{nd} and 4^{th} order slices. The 4^{th} order model resulted in a much more accurate segmentation than the 2^{nd} order model. This demonstrates the advantage of performing segmentations on higher order data especially in the areas of crossing fibers.

Fig. 4.6 displays the segmentation result of the corpus callosum from the lateral view. Many seeds were initialized to demonstrate that the 2^{nd} order model can produce an accurate segmentation when additional seeds are placed. The 2^{nd} order model produced a segmentation result similar to the 4^{th} order model. However, the 4^{th} order model still produced a qualitatively more accurate segmentation.

4.5 Discussion

The random walker segmentation algorithm can be extended to segment both 2^{nd} and 4^{th} order DT-MR images by utilizing appropriate tensor distance metrics. The segmentation

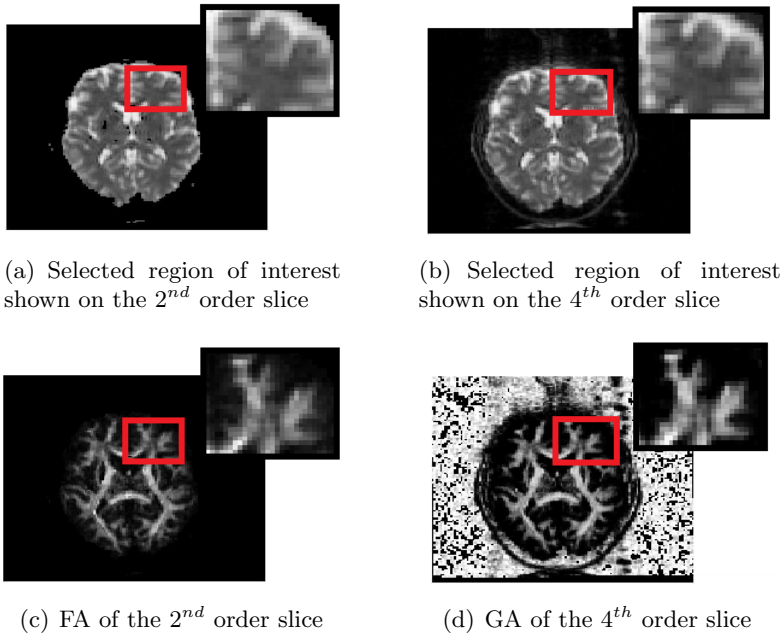

(a) Selected region of interest shown on the 2^{nd} order slice

(b) Selected region of interest shown on the 4^{th} order slice

(c) FA of the 2^{nd} order slice

(d) GA of the 4^{th} order slice

Figure 4.4: The selected slices and region of interest chosen for the segmentation

is carried out on a weighted graph, where tensor distance metrics that use the full tensor information are used to define edge weights. The normalized L_2 tensor distance is used to define the weights on the graph for the 4^{th} order tensor field segmentation whereas the Log-Euclidean is used for the 2^{nd} order tensor field segmentation.

The proposed approach is applied on both real and synthetic DT-MR images. The synthetic data set was constructed to demonstrate the limitation of the 2^{nd} order tensors to correctly represent fiber crossings. In all the experiments carried out, the 2^{nd} order tensor model lead to inaccurate and poor segmentation results in regions with complex fiber structures as compared to the segmentation results obtained from the 4^{th} order tensor data. This demonstrates the advantage of performing segmentation on higher order tensors.

Our segmentation results were very sensitive to the free β parameter that is used in Eq. 4.6 and also to the number of seeds initially placed by the user. This is especially the case for the 2^{nd} order tensor field segmentation where the placement of more seeds resulted in more accurate segmentations. This is a limitation of the underlying random walker segmentation technique. Future work will investigate how to automatically select a

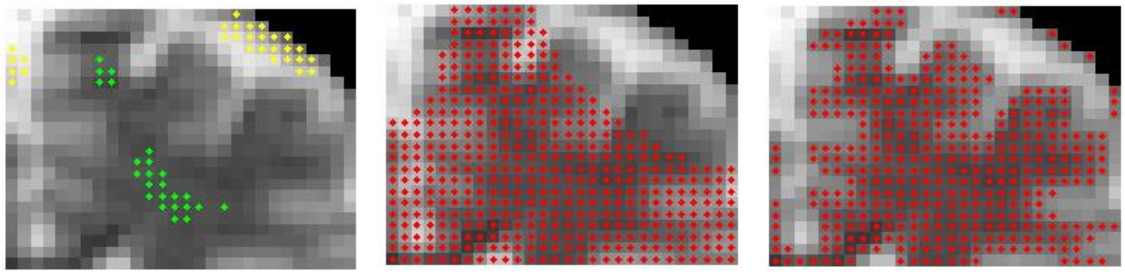

(a) Original image with seeds (b) 2^{nd} order segmentation result (c) 4^{th} order segmentation result

Figure 4.5: Segmentation result of the fibers performed on both the 2^{nd} and 4^{th} order slices.

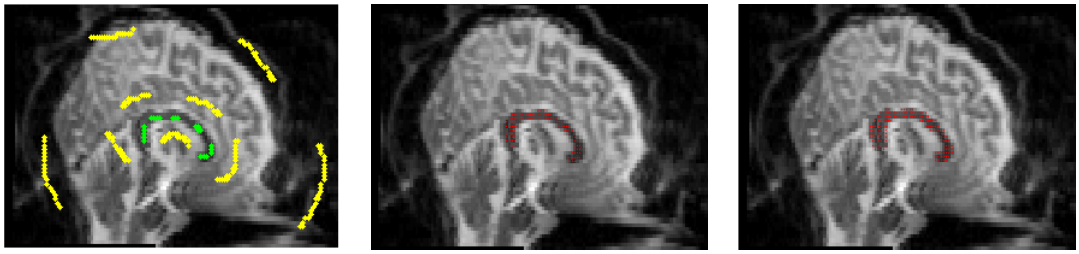

(a) Initial image with seeds (b) 2^{nd} order tensors segmentation (c) 4^{th} order tensors segmentation

Figure 4.6: Segmentation result of the corpus callosum from the lateral view. Demonstration of segmentation result when more seeds are initialized

suitable value for β and test the segmentation technique on more real datasets in addition to quantitatively compare the segmentation results obtained from 2^{nd} order and 4^{th} order tensor fields.

Chapter 5

Brain Tissue Discrimination

5.1 Introduction

DT-MRI has been used to describe the structural geometry of many types of tissue such as, muscle tissue, bone marrow, the heart and the brain. A 3x3 diffusion tensor can describe the degree and principle directions of anisotropic diffusion. Several scalar measures have been proposed that attempt to describe the diffusion anisotropy information provided by the tensors. The measures are useful for discriminating between healthy and damaged tissue micro structure [3].

A tensor **D** can be visualized as an ellipsoid with lengths of the three orthogonal principle axes proportional to the tensor's eigenvalues $\lambda_1, \lambda_2,$ and $, \lambda_3$ (in decreasing order). The sum of the eigenvalues is equal to the trace of the diffusion tensor ($\mathrm{tr}\,(D) = \lambda_1 + \lambda_2 + \lambda_3$). The tensor's eigenvectors $\hat{e}_1, \hat{e}_2$ and $\hat{e}_3$ describe the direction of the diffusion in the tensor.

Using symmetry properties of the ellipsoid the diffusion tensor can be decomposed into three basic geometric measures and can be represented using a combination of basis shapes. There are three different cases of diffusion [34],

1. Linear case ($\lambda_1 \gg \lambda_2 \cong \lambda_3$). Diffusion in this case is mainly in the direction of the largest eigenvalue,
$$D = \lambda_1 \hat{e}_1 \hat{e}_1^T \tag{5.1}$$
2. Planar case ($\lambda_1 \cong \lambda_2 \gg \lambda_3$). Diffusion is restricted to a plane spanned by two eigenvectors corresponding to the two largest eigenvalues
$$D = \lambda_1 \left(\hat{e}_1 \hat{e}_1^T + \hat{e}_2 \hat{e}_2^T \right) \tag{5.2}$$

3. Spherical case ($\lambda_1 \cong \lambda_2 \cong \lambda_3$). Diffusion in this case is isotropic

$$D = \lambda_1 \left(\hat{e}_1 \hat{e}_1^T + \hat{e}_2 \hat{e}_2^T + \hat{e}_3 \hat{e}_3^T \right) \tag{5.3}$$

The classification of diffusion into these three distinct types allows for the description of a diffusion tensor according to its geometry. Three shape measures are derived from these diffusion cases that describe how close the tensor is to the cases of line, plane and sphere. The measures quantitatively describe the geometrical shape of the diffusion tensors. The measures for linear(C_l) , planar (C_P) and spherical (C_S) are defined as follows[34],

$$C_L = \frac{\lambda_1 - \lambda_2}{\mathrm{tr}\,(D)} \tag{5.4}$$

$$C_P = \frac{2\,(\lambda_2 - \lambda_3)}{\mathrm{tr}\,(D)} \tag{5.5}$$

$$C_S = \frac{\lambda_3}{\mathrm{tr}\,(D)\,/3} \tag{5.6}$$

The measures range between 0 and 1 and their sum is 1. Therefore, only two of the measures for each tensor need to be calculated. Each of the measures when applied to brain tissue will reflect a different type of diffusion. For instance, when applied to white matter C_L accentuates the uniformity of tract direction within a voxel. Therefore, it will return a high value when diffusion is restricted to two orthogonal directions.

Several methods have been proposed to described diffusion anisotropy and relate it to the geometrical structure of tissue. The relative and the fractional anisotropy measures are two widely used anisotropy measures. The relative anisotropy (RA) is defined as follows,

$$RA = \frac{\sqrt{(\lambda_1 - \mathrm{tr}\,(D))^2 + (\lambda_2 - \mathrm{tr}\,(D))^2 + (\lambda_3 - \mathrm{tr}\,(D))^2}}{\sqrt{6}\ \mathrm{tr}\,(D)} \tag{5.7}$$

The Fractional anisotropy (FA) is another measure that is similar to RA and is defined as follows,

$$FA = \frac{\sqrt{3\,(\lambda_1 - \mathrm{tr}\,(D))^2 + (\lambda_2 - \mathrm{tr}\,(D))^2 + (\lambda_3 - \mathrm{tr}\,(D))^2}}{2\,(\lambda_1^2 + \lambda_2^2 + \lambda_3^2)} \tag{5.8}$$

FA is the most commonly used scalar diffusion anisotropy measure. It is a common metric used to describe the degree of diffusion directionality. A high FA value signifies that diffusion occurs predominantly along a single axes. On the other hand, a low FA value indicates diffusion along all three cardinal axes.

FA has been widely used for the diagnosis and assessment of degenerative brain diseases such as Multiple Sclerosis (MS) . It has been shown in [32] that FA is derived using a generalized tensor dot product in Euclidean space. However, recent studies have demonstrated that the space of diffusion tensors does not form a Euclidean vector space. Therefore Weldeselassie et al.[32] derive two new anisotropy measures that take into account the correct representative space of diffusion tensors. Just like FA they are based upon the eigenvalues of the diffusion tensor. The proposed metrics provide a measure of the tensor shape difference between the diffusion tensor and its closest isotropic tensor. Therefore, the anisotropy measures are referred to as the Shape Anisotropy Index (SA). The two measures differ in the distance metrics that they are derived from. The first measure is derived from the J-Divergence distance measure and is defined as follows,

$$SA_{JD} = \tanh\left(\sqrt{\sum_{i=1}^{3} \frac{(\lambda_i - \bar{\lambda})^2}{\lambda_i \bar{\lambda}}}\right) \tag{5.9}$$

where $\bar{\lambda}$ is the mean of the eigenvalues. The second measure is derived from the Log Euclidean distance measure and is defined as follows,

$$SA_{LE} = \tanh\left(\sqrt{\sum_{i=1}^{3} \log^2\left(\frac{\lambda_i}{\bar{\lambda}}\right)}\right) \tag{5.10}$$

The hyperbolic tangent scales the range of the measure to [0,1), which makes it possible to compare the results of the measure to FA and RA. It is apparent from the definitions of all the anisotropy measures that they behave differently, yet they all depend on the same set of parameters (λ_1, λ_2 and λ_3).

5.2 Contribution

In this chapter we compare the anisotropy measures FA, RA, SA_{JD}, SA_{LE} and the shape measure C_L to determine which measure can provide the best discrimination between different types of brain tissue. This work was published in SPIE 2011 [32]. The comparison is performed by calculating a detectability index for different regions in the brain from a segmented DT-MRI brain atlas. Moreover, we investigate the relationship between tissue architecture and MR frequency shifts using numerical simulations.

Section 5.3.1 explains the detectability index used to evaluate the different anisotropy measures and presents the DT-MRI segmented atlas used. The tissue discrimination results

are presented in section 5.4.1. Finally, the discussion and concluding remarks are made in section 5.5

5.3 Methods

5.3.1 Tissue Discrimination

For the task of discriminating between two tissue classes in the brain i.e. between gray and white matter, we use a measure of diffusion anisotropy A, which can be evaluated using a detectability index [3],

$$d = \frac{< A_1 > - < A_2 >}{\sqrt{\sigma_1^2 - \sigma_2^2}} \tag{5.11}$$

where $(< A_1 >, \sigma_1^2)$ and $(< A_2 >, \sigma_2^2)$ are the means and variances of the anisotropy values for the two tissue classes. The anisotropy measure with the greatest detectability index indicates that it can discriminate between two tissue classes the best. The variances depend upon a combination of tissue and subject variability, measurement noise, the encoding axes, the diffusion weighting and the pulse sequence parameters. In this case we compare the anisotropy measures FA, RA, SA_{JD}, SA_{LE} and the shape measure C_L.

Fig. 5.1 shows FA, RA, SA_{JD} and C_L maps for a selected DT-MR brain image slice. This dataset is publicly available by the John Hopkins Medical Institute Laboratory of Brain Anatomical MRI (http://Ibam.med.jhmi.edu/). We don't show SA_{LE} since, it is very similar to SA_{JD}. The four different maps look quite different, therefore it is expected that each anisotropy measure will discriminate between different tissue types differently.

Segmented Atlas

The detectability indicies for FA, RA, SA_{JD}, SA_{LE} and C_L are calculated for various types of tissue in the brain. We chose the following regions of interest to calculate the indicies:

- Corpus callosum (CC).
- Internal capsule (IC).
- Thalamus (TH).
- Gray matter (GM).

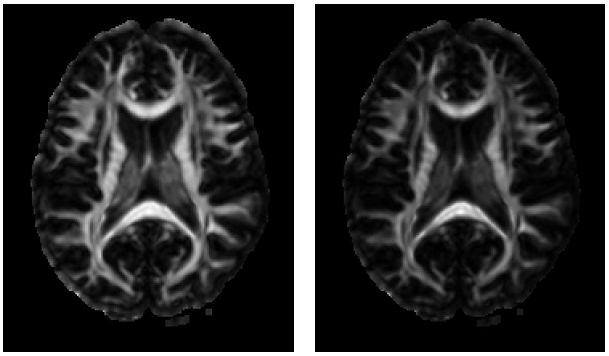

(a) FA (b) RA

(c) SA_{JD} (d) C_L

Figure 5.1: FA,RA,SA_{JD} and, C_L of a chosen DT-MR brain image slice

- Subcortical white matter (SCW).

We obtained a DTI atlas (JHU_MNI_SS) from John Hopkins Medical Institute Laboratory of Brain Anatomical MRI [1] which is registered to a white matter parcellation map (JHU_MNI_SS_WMPM_TypeI). The parcellation map is a hand-segmented map, in which known white matter structures are manually segmented based on FA and color (fiber orientation) information. Peripheral white matter regions (beneath the cortex) that are difficult to define manually were defined by white matter probability in some atlases. The entire brain is parcellated to 56 core and 46 peripheral white matter regions, in addition to 10 subecortical gray matters, hippocampi, and others (total 130 structures). Fig. 5.2(a) shows a single slice of FA with the parcellation map superimposed on it. From the parcellation

[1] http://Ibam.me.jhmi.edu/

map the 5 regions of interest (fig. 5.2(b)) were identified.

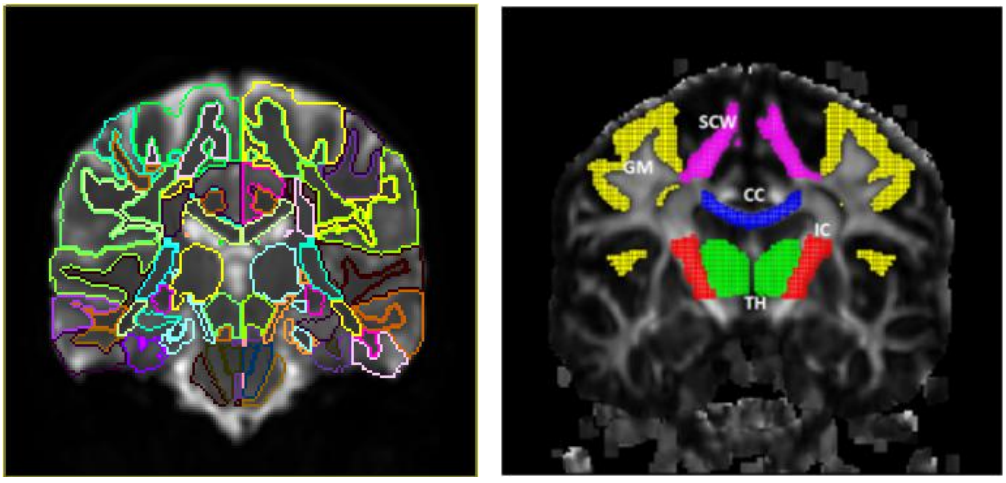

(a) Single slice of FA with the parcellation map superimposed on it

(b) Single slice of FA with the Regions of interest highlighted

Figure 5.2: A single slice of FA with corresponding regions of interest.

5.4 Results

Our tissue detectability results are presented in Table 5.1 where the highlighted values of d indicate that the anisotropy index given on that row performs best in discriminating tissue classes on the corresponding column. Since, the ability to distinguish between the tissue groupings by a specific anisotropy measure should increase with the magnitude of the detectability index.

None of the measure returned a highest detectability index across all of the tissue groupings. This shows that each anisotropy measure can be used according to the application at hand. For instance, FA showed higher detectability index values when discriminating between areas that are both within white matter. Whereas, SA showed higher detectability index values when discriminating between white matter and gray matter regions. The shape measure C_L showed the highest values in areas that are characterized with linear shaped areas (highly anisotropic).

Table 5.1: Estimated detectabilites, d, between selected tissue groups for the selected measures. The anisotropy measure with the greatest separability is highlighted.

	CC vs IC	CC vs TH	CC vs GM	CC vs SCW	IC vs TH	IC vs GM	IC vs SCW	TH vs GM	TH vs SCW	GM vs SCW
C_L	0.02	1.19	1.69	**0.67**	1.42	2.01	0.79	1.32	**0.67**	1.46
RA	0.16	**0.96**	1.76	0.56	1.40	2.37	0.85	1.99	0.48	1.69
FA	0.24	0.95	2.01	0.52	**1.46**	2.69	**0.86**	2.07	0.45	1.82
SA_{JD}	**0.39**	0.74	**2.12**	0.36	1.35	**2.89**	0.81	2.10	0.36	**1.90**
SA_{LE}	0.38	0.73	2.10	0.37	1.33	2.87	0.82	**2.11**	0.34	1.89

5.4.1 Tissue Discrimination Results

5.5 Discussion

Diffusion tensor measurements of brain tissue provide us with a wealth of information about the tissue's structure. The eigenvalues of a diffusion tensor can be used to explain the shape of the tensor. Several measures of tensor anisotropy have been proposed where each measure is a function of the three eigenvalues. From our experimental results, it is clear that each of the anisotropy measures emphasize different tensor features. We chose to examine four measures of diffusion tensor anisotropy and one shape measure. The experiment can be extended to any anisotropy measure. Some measures were better than others in discriminating between different tissue types. In general, FA performs better in detecting differences among tissues within the white matter whereas, SA detects differences between white matter and gray matter. Therefore, anisotropy measures should be chosen according to the application they are used for.

Chapter 6

A Novel Segmentation Approach for Mammograms

6.1 Introduction

The segmentation of the breast area from mammograms is a crucial and initial pre-processing step for computer aided diagnostic tools. Existing segmentation approaches on mammograms suffer from several problems and have specific modes of failure. Most existing approaches fail on images that exhibit a large amount of noise and on images where the breast edge isn't well defined and has low contrast with the background.

There are several proposed techniques that have been used to segment mammograms [27]. In many cases histogram techniques are used to segment the breast region from the background. These techniques involve a global basic thresholding of the mammogram and are the simplest of all the segmentation techniques. A threshold value can be either automatically estimated or supplied by the user. This approach has many modes of failure especially when artifacts are present or when the background is noisy. Masek et al.[22] use local thresholding instead of a global thresholding technique and have shown promising and improved results. On the other hand, Abdel-Mottaleb et al.[2] use a system of masking images with different thresholds to find the breast edge. They calculate the gradients from the images to estimate the approximate location of the skin edge. This method is restricted to the number of mask images created and the number of thresholds used. Of the 500 mammograms tested, an "acceptable" boundary was found 98% of the time.

Gradient based methods have also been used to detect the breast edge. Such approaches involve the usage of spatial or edge detection filters such as Sobel or Laplacian. A global thresholding technique is used to obtain the preliminary region which is then processed using a filter. This approach does not tend to be robust since, the edge of the breast has low contrast with the background which makes it a challenge to detect the skin edge using a filter. Moreover, the breast edge is a contour and does not have a strict horizontal or vertical orientation. Mendez et al.[23] find the breast contour using a gradient based method. A thresholding technique is used to isolate the breast region of the mammogram. The mammogram is then divided into three regions using a number of automatically determined reference points and a tracking algorithm that tracks changes in the gradient in those regions is applied. The algorithm was tested on 156 mammograms and an "acceptable" boundary was found 89% of the time.

Bick et al.[10] propose an approach that involves thresholding, region growing and morphological filters. The mammogram is initially filtered to reduce noise and then a texture operator is applied. Morphological filters are used to eliminate irregularities along the breast contour and contour tracing extracts the breast contour. The algorithm was tested on 740 mammograms with a 97% "acceptable" rate.

A promising and intuitive approach to the segmentation of mammograms is the usage of polynomial modeling based techniques[12]. A histogram threshold is performed to enhance the response of non dark pixels, then the boundary is smoothed using cubic B-splines. Samples at fixed intervals are extracted and a smooth curve is generated through cubic polynomial calculations [29]. This approach relies heavily on the initial detection of the curve and requires user input to define the initial point of the boundary. Therefore, it can't be incorporated in a fully automatic segmentation approach.

Active contours (snakes) have also been used for the detection of the breast contour [36], where an evolving curve starts from an initial point and evolves to include the whole edge of the breast. Active contours tend to be sensitive to noise and weak edges, which make them a poor candidate for the segmentation of the breast region. They also rely heavily on the initialization point of the snake.

Oliver et al [24] present a statistical approach which also incorporates spatial information for the segmentation of the breast area. The approach is based on modeling a set of patches of either fatty or dense parenchyma using statistical techniques. The modeling is performed using principle component analysis (PCA) and linear-discriminant based (LDA) techniques.

After the models are created, each pixel of a new mammogram is classified as being fatty or dense tissue.

A major difference between all the approaches listed above lies in the domains on which the hypothesis, tests and decisions are based. The approaches all have certain drawbacks. The usage of filters, only makes use of local information and doesn't always produce connected closed edge contours. Snake models make use of only the information along the boundary and require accurate initialization points. Region growing techniques have the advantage of evaluating the statistics inside a confined region. However, the result of the segmentations sometimes suffer from irregular boundaries and small holes.

6.2 Contribution

In this chapter, we present a novel statistical framework for the segmentation of the breast area from mammograms. It is derived by automatically identifying intensity values that can be used to define a probability distribution that describes the breast area. This, in turn is used as a classifier to determine if a pixel belongs to the breast area. The algorithm incorporates both local and global information and it takes into account the intensity variability of the breast area. The mammogram is first thresholded using a clustering thresholding algorithm that serves to separate the image into four non overlapping clusters, therefore returning three threshold values. The regions can be identified as: background, low intensity, medium intensity and high intensity. The purpose behind performing this multi level thresholding is because of the inherent nature of mammograms. The four clusters resulting from the thresholding method can be described as follows: (i) The background (ii) A low intensity region which includes the breast's skin line. (iii) The medium intensity region contains the majority of breast tissue. (iv) The high intensity region contains noise artifacts, external labels, implants, external devices and the high intensity regions in the breast such as calcifications.

The three regions (excluding the background) are then used to automatically calculate three separate "seed" values that are used to create three different probability distributions. The distributions are visualized as images (kernel images) where each value in the image represents a degree of membership to a seed. A higher value means a higher probability of belonging to the seed. As a post processing step the largest connected component is detected which is assumed to be the breast region. This is a safe assumption since the

breast is always the largest component in a mammogram. Fig. 6.1 graphically displays the steps of the algorithm.

Section 6.3.1 presents the thresholding part of the algorithm. Section 6.3.2 describes the process of determining the seed values. Section 6.3.3 explains how the kernel images are calculated and produced. The connected component detection used is described in section 6.3.4. The segmentation results are presented in section 6.4. Finally, concluding remarks are made in section 6.5.

6.3 Methods

6.3.1 Histogram Clustering Thresholding

The purpose of thresholding is to separate an image into multiple non overlapping segments. The task of thresholding mammograms tends to be challenging because mammograms lack large areas of uniform intensity especially when the background is noisy. Otsu's thresholding method [25] uses discriminant analysis to separate an image's histogram into distinct classes. The method evaluates the goodness of every possible threshold value by maximizing a criterion function. The criterion function is maximized if the means of two classes are separated as far as possible and their variance is as minimum as possible.

The multi-level thresholding algorithm implemented in our framework is based on Otsu's thresholding method and was proposed by Arifin and Asanao [4]. The proposed method is based on the idea of histogram bin clustering. Since, thresholding can be viewed as a clustering problem. The method can be visualized as developing a dendrogram of gray levels in the histogram of an image based on a similarity measure. The measure takes into account the inter variance, intra variance and means of clusters. Fig. 6.2 shows a histogram of a 11x11 sample image that contains 43 gray levels. The dendrogram in Fig. 6.2(b) provides a visualization of the clustering process. The numbers on the horizontal axis of the dendrogram are the indices of the gray levels (1 to 43), whereas the height of the links between the clusters represent the order of the clustering. Finally, the threshold value is the index that separates the $t-$clusters from each other. The dendrogram in Fig. 6.2(b) is a result of a $2-$level thresholding hence, there are 2 clusters. Whereas, the thresholding performed on the mammograms is a $4-$level thresholding, resulting in four clusters and three thresholding values.

Arifina and Asano's t-level thresholding algorithm can be detailed as the following:

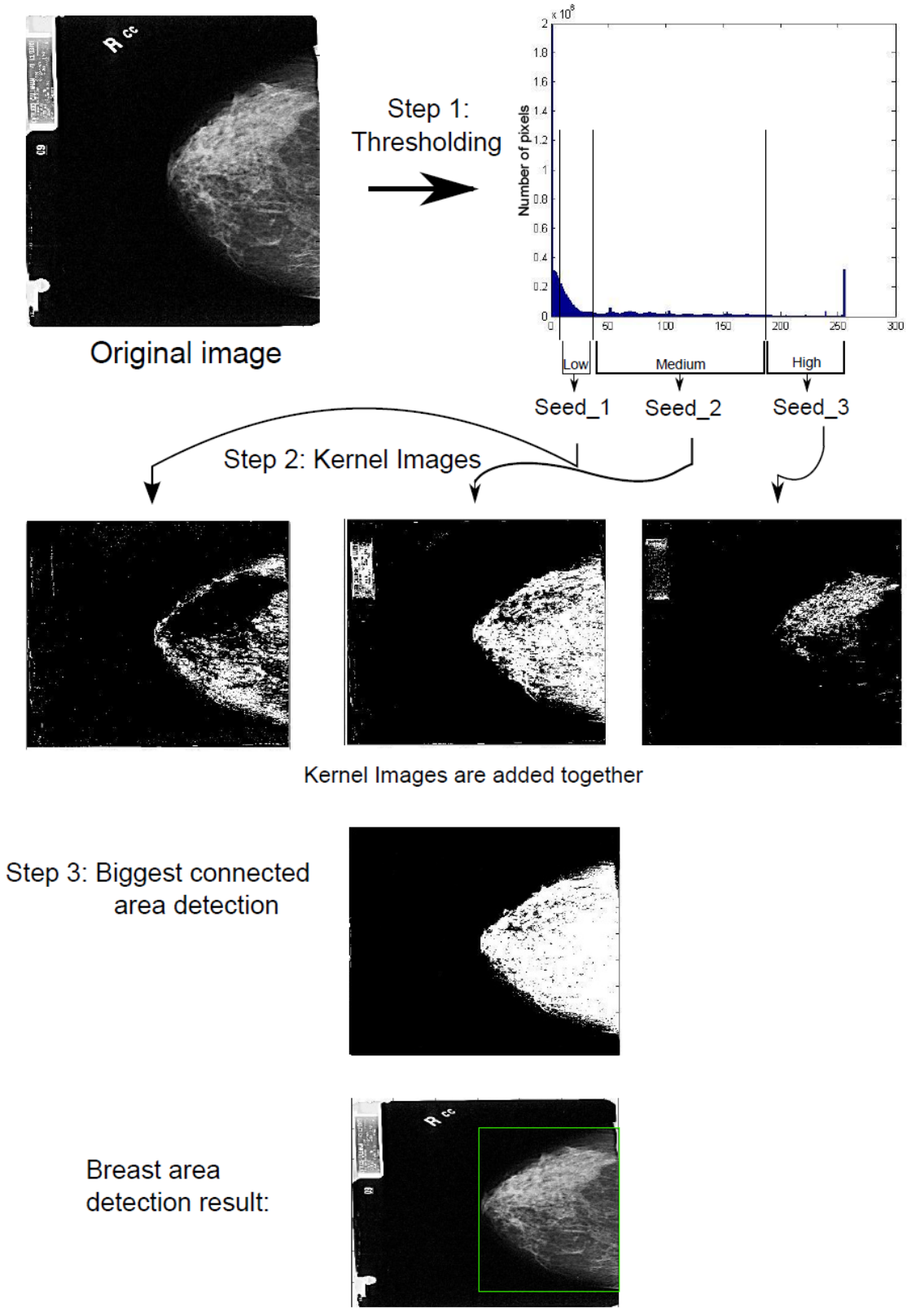

Figure 6.1: A graphical description of the algorithm, showing its steps.

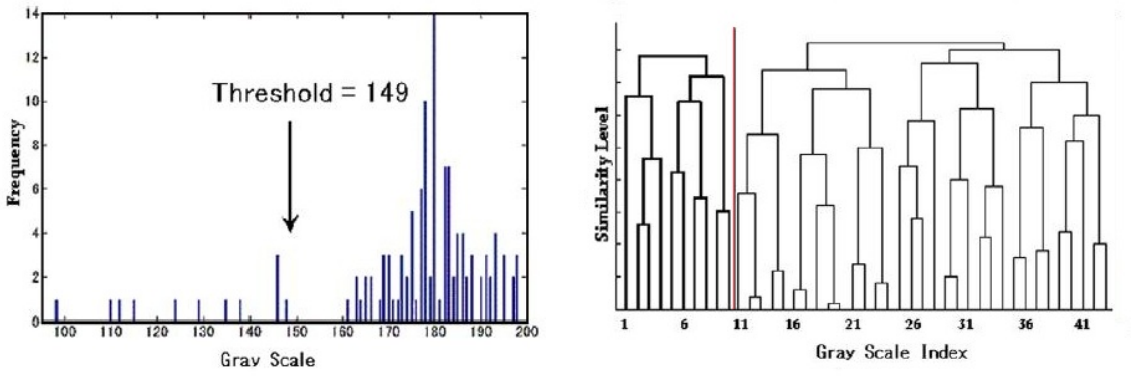

(a) (b)

Figure 6.2: Histogram of a 11x11 sample image with 43 gray levels and a visualization of its corresponding dendrogram. This figure was obtained from [4]

1. Initially every non empty gray level is regarded as a cluster. i.e. if a histogram has K initial non empty gray levels then there are K initial clusters.
2. The following two steps are repeated until t-clusters are obtained.
   (a) The similarities between adjacent clusters are computed using a distance measure.
   (b) The pair with the smallest distance are merged into one cluster.
3. The intensity values separating the clusters are identified as the thresholding values.

Distance Measurement

The distance between two adjacent clusters provides a measure of how similar two clusters are. The smaller the distance, the higher the similarity between the two clusters. The measurement is based on both the difference between the means of the two clusters and the variance of the resulting cluster.

The histogram is viewed as a probability density function. Let $h(z)$ be the histogram of the target image where z indicates the gray level. The histogram $h(z)$ gives the occurrence frequency of the pixel with gray level z. So we can define $p(z) = h(z)/N$ where N is the number of pixels in the image. $p(z)$ is then the probability of the occurrence of the pixel with gray level z. Another function is defined which indicates the occurrence probability of

pixels belonging to a cluster C_k

$$P(C_k) = \sum_{z=T_{k_1}}^{T_{k_n}} p(z), \sum_{k=1}^{k} P(C_k) = 1 \tag{6.1}$$

where T_k is the intensity value in the cluster C_k. So basically the function $P(C_k)$ is the sum of the occurrence probability of each intensity value in a cluster k.
The distance function used is defined as follows[4]:

$$Dist(C_{k_1}, C_{k_2}) = \sigma_a^2(C_{k_1} \cup C_{k_2}) \sigma_I^2(C_{k_1} \cup C_{k_2}) \tag{6.2}$$

where $\sigma_a^2(C_{k_1} \cup C_{k_2})$ is the intra class variance of two merged clusters, $\sigma_I^2(C_{k_1} \cup C_{k_2})$ is the inter class variance, $m(C_k)$ is the mean of the cluster C_k. The inter-class variance takes into account the probability occurrence of both clusters and the difference between their means. It is defined as follows:

$$\sigma_I^2(C_{k_1} \cup C_{k_2}) = \frac{P(C_{k_1}) P(C_{k_2})}{(P(C_{k_1}) + P(C_{k_2}))^2} (m(C_{k_1}) - m(C_{k_2}))^2 \tag{6.3}$$

$m(C_k)$ is the mean of cluster C_k, defined as follows:

$$m(C_k) = \frac{1}{P(C_k)} \sum_{z=T_{k_1}}^{T_{k_n}} z * p(z) \tag{6.4}$$

The intra-class variance $\sigma_a^2(C_{k_1} \cup C_{k_2})$ is the variance of all the pixel values in the merged cluster and is defined as follows:

$$\sigma_a^2(C_{k_1} \cup C_{k_2}) = \sum_{z=T_{k_1}}^{T_{k_n}} \left((z - M(C_{k_1} \cup C_{k_2}))^2 p(z) \right) \tag{6.5}$$

In our implementation a 4-level histogram clustering is used. Therefore, separating the histogram into four clusters and returning three threshold values. The first cluster is assumed to contain the background pixels, the second cluster contains the low-intensity range of the breast, whereas the third cluster contains most of the breast tissue and the fourth cluster contains the high intensity regions of the breast and external objects.

6.3.2 The Determination of the Seed Values

The seeds are three automatically determined intensity values that will later serve to calculate a probability density distribution. Each seed represents a region of the breast tissue.

The first seed is a low intensity value representing the breast's skin line, the second seed is a medium intensity value representing the main breast tissue and the third seed is a high intensity value that takes into account the high intensity regions of the breast such as calcifications.

The output of the thresholding algorithm is three threshold values which separate the image's histogram into four regions. The first threshold value separates the breast from the background. The first region of interest constitutes of all the pixels that have an intensity value less than the second threshold intensity value and greater than the first. The first seed is defined as the center value of the region as demonstrated in equation 6.6. This seed value is used represent the low intensity region of the breast.

$$\text{Seed 1} = \text{Threshold value 1} + (\text{Threshold value 2 - Threshold value 1})/2 \tag{6.6}$$

The second region of the histogram constitutes of all the pixels that have an intensity value greater than the second threshold intensity value and less than the third threshold level. The second seed is simply the second threshold intensity value. This is the intensity area where most of the breast tissue is present in and is free from any background or artifact pixels.

The third region of the histogram constitutes of all the pixels that have an intensity value greater than the third threshold value. Labels, wedges and noise are present in this area of the histogram. Such artifacts have very high intensity values that are not present in the breast tissue and are present at the end of the histogram. The presence of artifacts in a mammogram corresponds to the presence of a peak at the end of the histogram. Fig. 6.3 shows a mammogram and it's corresponding histogram. Note the large peak at the end of the histogram corresponding to the wedge and label's present on the mammogram. The seed value for this region is calculated as the following,

$$\text{Seed 3} = \text{Threshold value 3} + (256\text{- Threshold value 3})/2 \tag{6.7}$$

The result of this is a set of three intensity values referred to as seeds: low intensity, medium intensity and high intensity. All three of the seeds are detected automatically with no user specified parameters involved.

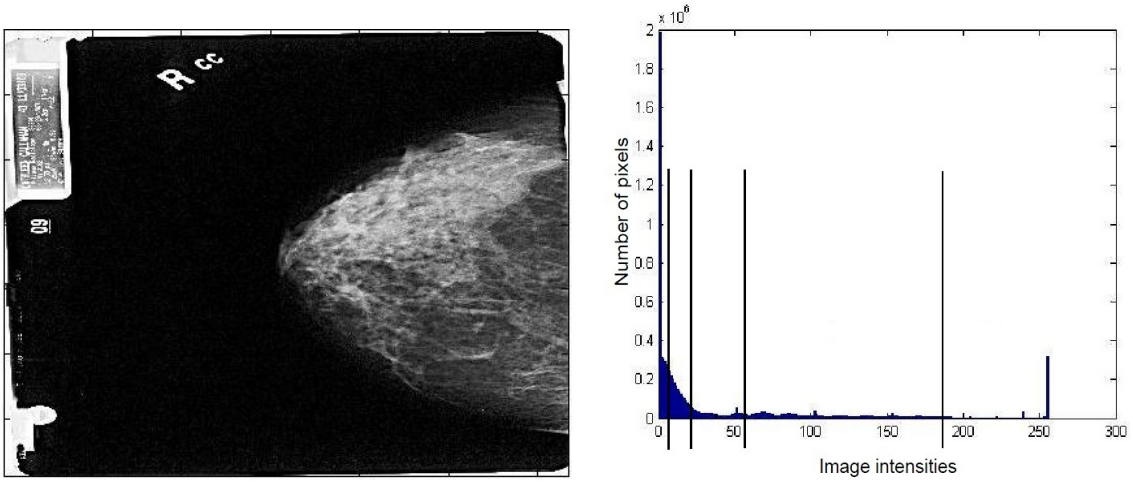

(a) Original Mammogram

(b) Histogram of the mammogram sectioned into the corresponding intensity regions

Figure 6.3: A mammogram with it's corresponding histogram segmented into the intensity regions used to calculate the seed values.

6.3.3 Kernel images

The seeds are used to produce a "kernel" image, which is the result of applying a Gaussian probability distribution kernel on the image:

$$h(x,y) = P\left(I\left(x,y\right)|\left(seed,\sigma\right)\right) = \frac{1}{\sqrt{2\pi\sigma}}\ \exp\ -0.5\frac{\left(I\left(x,y\right)-seed\right)^2}{\sigma} \tag{6.8}$$

where σ is the variance and $I\left(x,y\right)$ is a pixel at position x,y. The function describes the probability that a pixel $I\left(x,y\right)$ can be generated by a Gaussian distribution $N\left(seed,\sigma^2\right)$. A more sophisticated probability could be used, but for our purposes this Gaussian kernel is sufficient. The purpose of performing this is to create a membership metric. If the pixels are close in intensity value to the seed, they will have a high kernel value whereas, if they are different the kernel value will be close to zero. By creating three kernel images, we are capturing the membership of the three different regions in the image.

The first distribution is centered around the first seed represents the pixels corresponding to the skin line. The distribution's variance (σ_1) is calculated as follows,

$$\sigma_1 = \text{(Seed 1 - Threshold value 1)}/2 \tag{6.9}$$

The second distribution centered around the second seed represents the pixels corresponding to the bulk of the breast tissue. The variance in this region (σ_2) is the largest since we assume that all the pixels in this region belong to the breast.

$$\sigma_2 = (\text{Seed 2 - Threshold value 2})/2 \tag{6.10}$$

The third and final distribution centered around the third seed represents the pixels corresponding to the high intensity regions in the breast. The variance (σ_3) in this region is calculated as follows

$$\sigma_3 = (\text{Seed 3 - Threshold value 3})/2 \tag{6.11}$$

An example of three kernel images is displayed in Fig 6.4. The three seed values used to produce the three kernel images are 20, 62 and 91 respectively. Each pixel in the three images has a kernel value, however the pixels with the higher kernel values have a higher intensity value and appear as bright pixels. Note how the first kernel image (Fig 6.4(b)) captures the skin line accurately and distinguishes it from the background and the rest of the breast tissue.

6.3.4 Largest Connected Component

As a post processing step to reach to the final segmentation solution we detect the largest connected component and return that as the breast region.

Connected component detection

The final segmentation result is returned by detecting the biggest connected component in the sum of the kernel images (the resulting image from adding the three kernel images). Since, the algorithm does not incorporate any spatial information there is a chance that some noisy areas could be classified as regions belonging to the breast tissue. An example of this case is displayed in Fig. 6.5 where the labels on the mammogram were classified as part of the breast.

A connected component labeling algorithm is used to detect the largest component. This approach consists of assigning a unique label to each maximal connected region of foreground pixels.

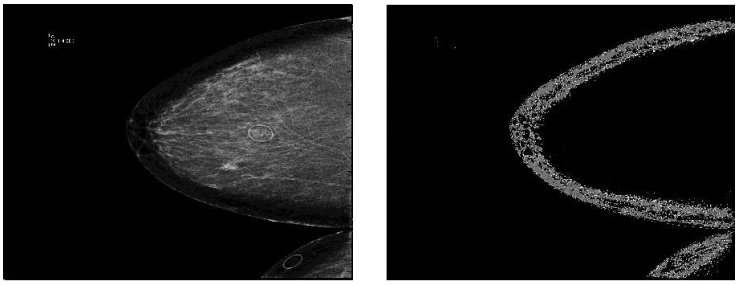

(a) Original image

(b) Low intensity kernel image

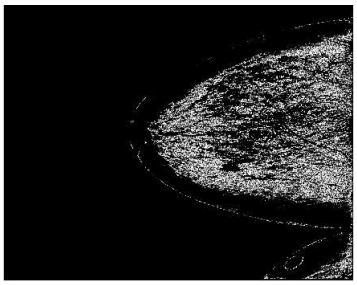

(c) Medium intensity kernel image

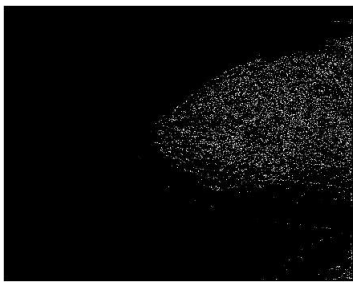

(d) High intensity kernel image

Figure 6.4: A mammogram and its corresponding kernel images.

Connected components labeling

Stedano and Bulgarelli [13] propose a simple and efficient connected components labeling algorithm which we use in our implementation.

Let I be the binary image resulting from the segmentation and F, B the non overlapping subsets of I corresponding to foreground and background respectively. A connected component C of I is a subset of F such that all the pixels in C are connected. Note that instead of iterating on all the pixels in the binary image we treat each region block as a pixel which reduces the computational complexity significantly. However, each region will be referred to as pixel in this section.

The algorithm generates a new image in which a unique label is assigned to pixels belonging to the same connected component. The background pixels remain untouched and only the foreground pixels are assigned labels. The labels are assigned by performing two raster scans. During the first scan, labels are assigned to each pixel based on the values of its neighbors. In this implementation a 4-connectivity neighborhood is used where x is the

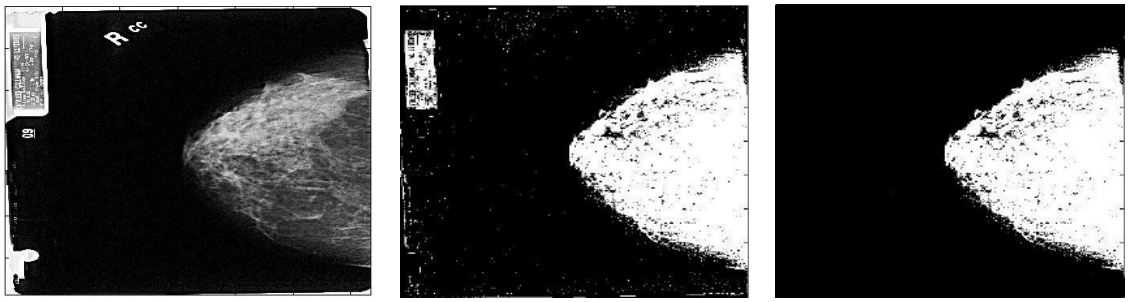

(a) Original Image (b) Sum of the kernel images (c) Result of the largest connected component detection

Figure 6.5: A mammogram, sum of the kernel images and the largest connected component detection result.

pixel to be labeled (Fig. 6.6). The algorithm can be described using the following cases. For

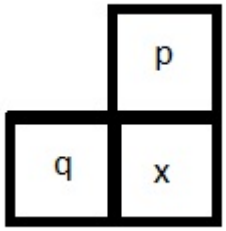

Figure 6.6: Demonstrating a 4-connectivity neighborhood where x is the pixel to be labeled.

all the foreground pixels in the image where x is the pixel to be labeled and its neighbors are p, q:

1. If the neighbors of the pixel x are both background pixels then x is assigned a new label.
2. If the neighbors both have the same label, then assign x that label.
3. If one of the neighbors is a background and the other has a label assign x that label.
4. If both neighbors have a different label then x is assigned either label and the two labels

are regarded as equivalent. This equivalence is stored in an array and is constantly updated during the scan. For instance (Fig. 6.7), if p had a label value of 1, and q had a label value of 2 then a common label needs to be decided upon to label x. This is done by setting one of the labels to be a survivor and the other is deleted (in this case assume $p's$ label is retained). The equivalence of the two labels is saved in a simple data structure such as an array which can keep track of the labels that are merged into one. During the second raster scan the equivalences that are stored in the array are applied to the labeled image, so that in the second scan $q's$ label would change from 2 to 1.

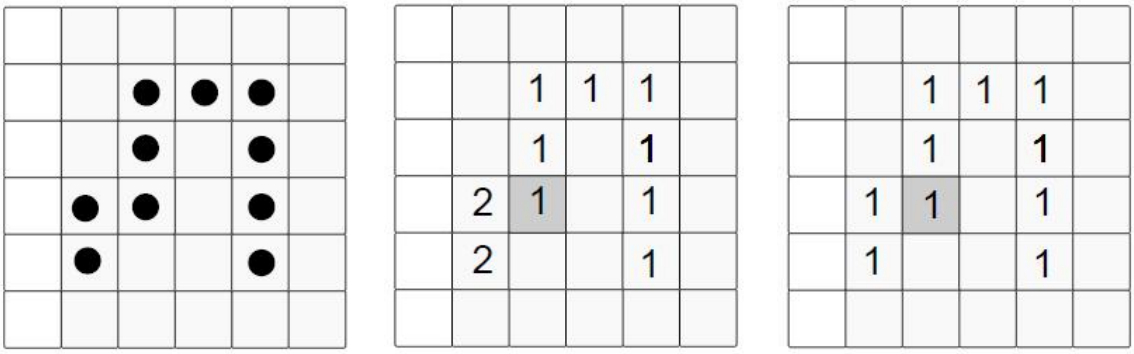

(a) Example image (b) Labeling result of the first scan (c) Labeling result of the second scan

Figure 6.7: An example of the labeling process. The circles in Fig. 6.7(a) represent the foreground pixels.

6.4 Results

The algorithm was tested on 300 mammograms which were reduced in resolution to 8-bit to make the segmentation process faster. The dataset consists of a wide range of cases i.e: digitized images, scanned images, images with labels and images with foreign objects such as clips and breast implants. The algorithm failed on two specific cases that will be described in the next section.

6.4.1 Segmentation Results

In this section, a subset of the results of applying the segmentation algorithm on the mammogram images are displayed. For each result four images are displayed:(i) The original mammogram. (ii) The summation of all three kernel images after the largest connected area is detected (iii) The detected breast region, where a yellow box is used to display the region detection result.

Fig. 6.8 shows the detection of the breast region from a scanned mammogram film. The breast region is a challenge to detect in scanned mammograms because they have noisy backgrounds and contain foreign labels. The intensity range of the labels is similar to the breast tissue and therefore it can be a challenge to distinguish them from the breast tissue. Our implementation detected the breast region accurately and didn't include the labels and foreign objects as part of the segmentation result.

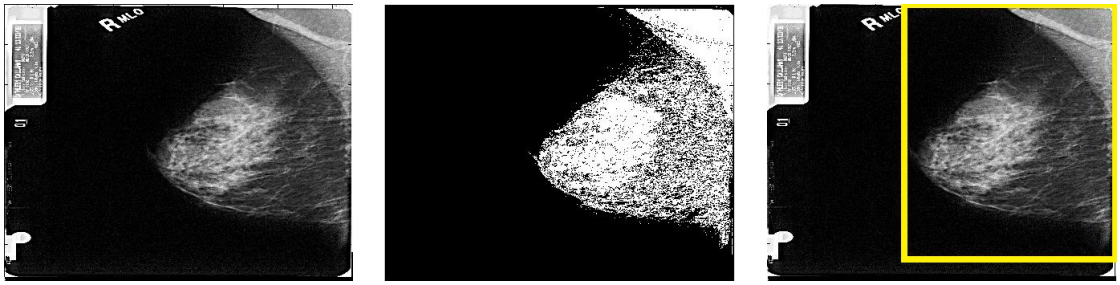

(a) Original Image

(b) Addition of kernel images (biggest connected area detected)

(c) Detected breast region

Figure 6.8: Segmentation of the breast region from a scanned mammogram.

Some mammograms contain external objects that overlap the area of the breast such as clips. Fig. 6.9 displays the breast area detection from such a mammogram image. The segmentation approach detected the breast region accurately and did not include the clips as part of the segmentation result.

Fig. 6.10 shows the segmentation result on another mammogram that contains an external clip. Again the segmentation approach detected the breast region accurately and did not include the clip as part of the segmentation result.

Fig. 6.11 displays the segmentation result on a mammogram that is inverted. This is

(a) Original Image

(b) Addition of kernel images (biggest connected area detected)

(c) Detected breast region

Figure 6.9: Segmentation of the breast region from a mammogram with external objects (clips).

the case for some mammograms where the background is assigned a high intensity value and the breast tissue has a low intensity range. The breast area was detected accurately. This demonstrates the robustness of the segmentation approach and its ability to handle inverted images.

Fig. 6.12 displays the segmentation result on a mammogram of a breast which contains an implant. The breast tissue is accurately distinguished from the implant. This again demonstrates the effectiveness of the algorithm in excluding external objects from the segmentation result and differentiating them from breast tissue.

6.4.2 Failure Cases

There were two specific cases in which the algorithm failed to detect the breast region correctly. The first case is demonstrated in Fig. 6.13. In this case, the breast tissue is separated by a clip which leads to the failure of the biggest connected component detection to correctly return the whole breast area as a result.

Whereas the second mode of failure is on mammograms where the whole of the image represents breast tissue and there is no background. Therefore the thresholding of the image into multiple regions and disregarding the background intensities is meaningless since there is no background. This case is demonstrated in Fig. 6.14.

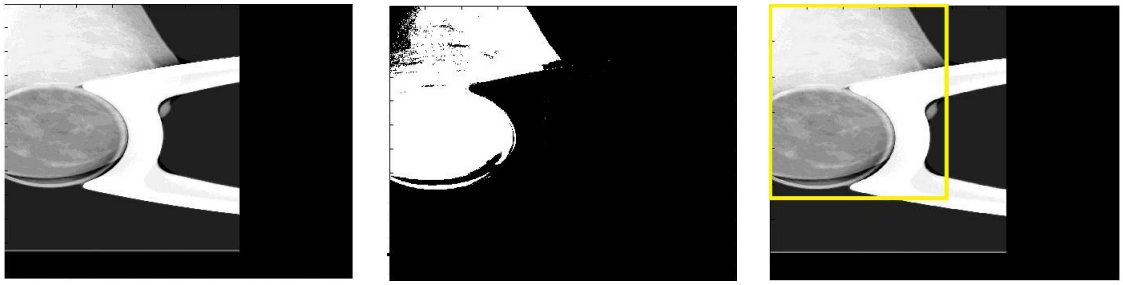

(a) Original Image

(b) Addition of kernel images (biggest connected area detected)

(c) Detected breast region

Figure 6.10: Segmentation of the breast region from a mammogram with external objects (clips).

6.5 Discussion

The segmentation of the breast area from mammograms can be a challenge because of the lack of uniform intensity regions, noisy backgrounds, presence of foreign objects and the low contrast nature of mammograms. The proposed novel segmentation approach for the detection of the breast area in mammograms overcomes those challenges. The segmentation is arrived at by automatically identifying intensity values that can be used to define a probability distribution that describes the breast area. The probability distribution is treated as a membership metric to distinguish breast tissue from the background and external foreign objects.

The breast region was tested on 300 mammograms and failed on two specific cases. In some instances, the labels are detected as breast tissue and therefore a post processing step that detects the largest connected component is implemented as part of the segmentation framework. The approach requires no pre-processing steps or any filtering operations which are computationally intensive. Moreover, it is completely automatic and requires no pre knowledge about the orientation of the breast images or the intensity levels in the images.

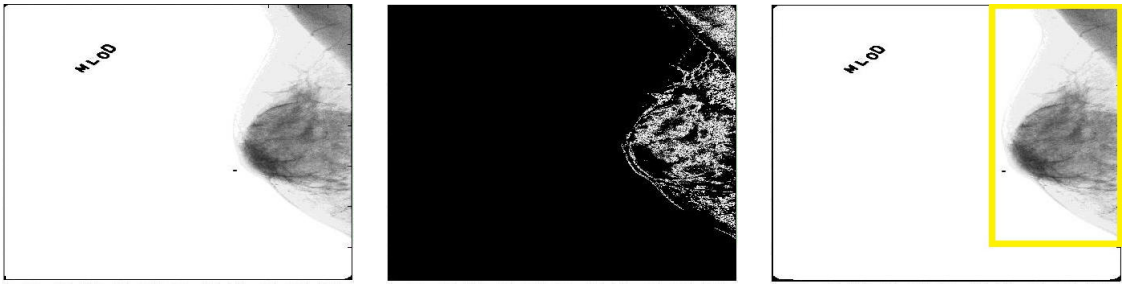

(a) Original Image (b) Addition of kernel images (biggest connected area detected) (c) Detected breast region

Figure 6.11: Segmentation of an inverted mammogram.

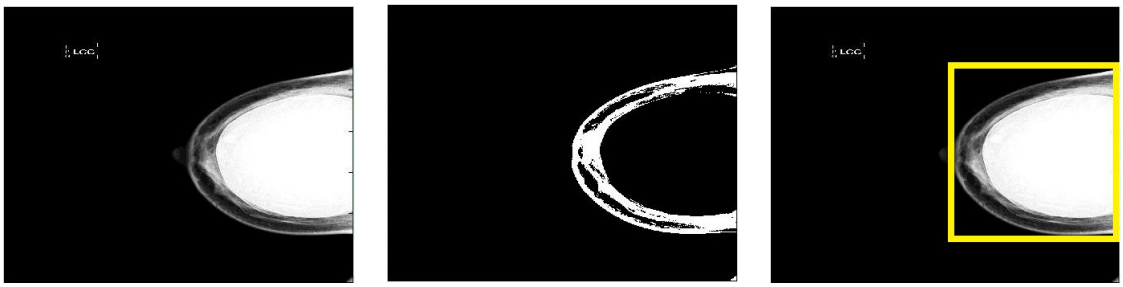

(a) Original Image (b) Addition of kernel images (c) Detected breast region

Figure 6.12: Segmentation of the breast region from a mammogram of a breast containing an implant.

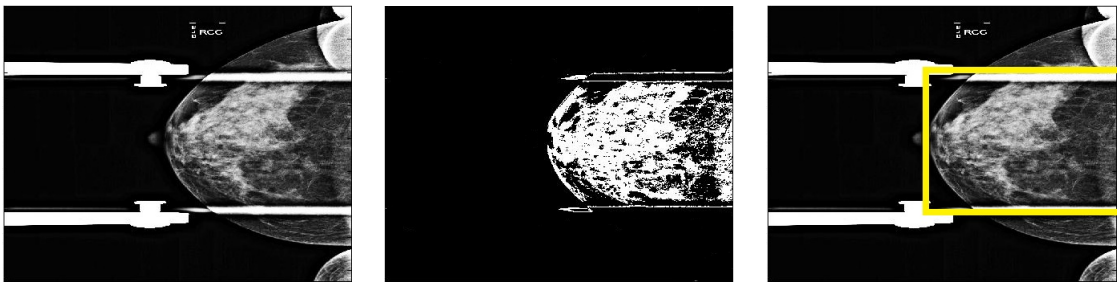

(a) Original Image (b) Addition of kernel images (c) Detected breast region

Figure 6.13: Segmentation of the breast region from a mammogram where a clip overlaps the breast and separates it into multiple sections.

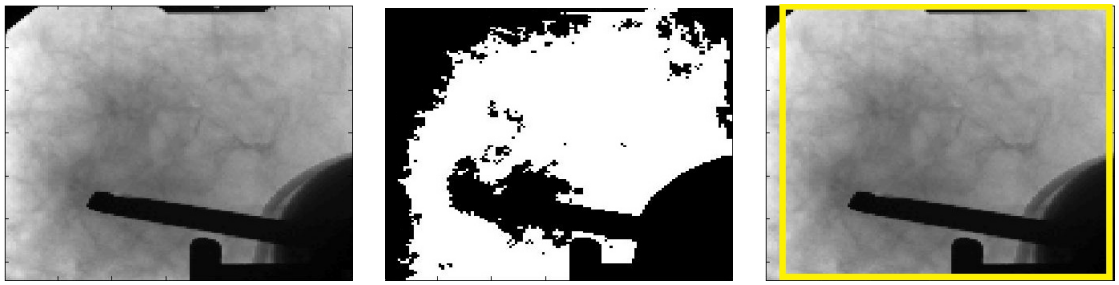

(a) Original Image (b) Addition of kernel images (c) Detected breast region

Figure 6.14: Segmentation of the breast region from a zoomed in view on the breast tissue

Chapter 7

Conclusion and Future Work

7.1 Conclusion and Summary

We have successfully extended the random walker segmentation algorithm to both 2^{nd} and 4^{th} order DT-MRI data. Moreover, we investigate the ability of different anisotropy measures to distinguish between various tissue in the brain. We also propose a novel segmentation framework for the detection of the breast area in mammograms. Our specific contributions are as follows:

- We applied the random walker segmentation algorithm to DT-MRI data, and we incorporated prior models in its formulation to allow the segmentation of disconnected objects. We used two DT-MRI distance metrics to evaluate the difference between tensors on the constructed graph which the segmentation is applied to. The two distance metrics are the Log euclidean and the J-Divergence. The advantage of using these two metrics is that they use the whole information contained in the tensors (both direction and magnitude). The segmentation results were compared to segmentation results obtained from using the graph cuts segmentation method. We show that the random walker returns more accurate results than the graph cuts.

- The random walker segmentation algorithm is also applied to higher (4^{th} order DT-MRI data. For 4^{th} order data we use the normalized L2 distance to evaluate the difference between tensors. The goal was to investigate if performing segmentations on higher order data has any advantages over 2^{nd} order data segmentations. The

results confirmed that 4^{th} order segmentations are more accurate especially in areas where fiber crossing is present.

- There are several different anisotropy measures that attempt to capture the geometric nature of tissue's micro structure. We investigate how each measure behaves differently with respect to distinguishing between different types of tissues in the brain. We compare FA,RA,SA and a shape measure C_L by computing a detectability index for different regions in the brain. The regions in the brain are identified from a segmented DTI brain atals. We arrive to the conclusion that FA performs better in detecting differences among tissue within the white matter where as SA detects differences between white matter and gray matter. The results show that each anisotropy measure should be chosen according to the applications to which it could be applied.

- Finally, a novel segmentation framework for the detection of the breast area in mammograms is developed. The segmentation algorithm automatically identifies intensity values that can be used to define a probability distribution that describes the breast area. This probability distribution is used as a classifier to determine if a pixel belongs to the breast area.

7.2 Future Work

There are multiple avenues of future work that may improve the results of this thesis and further validate our conclusions. Some of the more significant one are as follows,

- Extend the random walker implementation to produce 3D segmentations. The results of the 3D segmentations could be used to study the shape of the object segmented. This could also be used to validate the results of the segmentations. The extension would involve seeding the desired foreground object in all the slices in the DT-MRI data set and selecting an appropriate β parameter.

- The segmentation results from the random walker segmentation on DT-MRI data can be quantitatively validated if ground truth segmentations were obtained. This would give a better estimation of the performance of the segmentation algorithm. Moreover, the role of the free parameters could be further investigated, and ways of minimizing their effects on the segmentation result.

- Extend the random walker segmentation algorithm so that user supplied seeds are not required. Therefore, making it a fully automated segmentation technique which would extend the number of applications in which it could be applied to.
- Apply the random walker segmentation technique to track fibers in the brain. Fiber tracking is a new emerging area where the random walker segmentation method could be used to identify different types of fibers in the brain.
- It would be interesting to investigate whether the different anisotropy measures could be advantageous to different clinical applications. For instance, investigating if using SA in a certain clinical application would be better than using FA.
- Our current breast detection algorithm does not provide a contour outlining the skin line it just returns the region of the breast. Extending the algorithm to detect the skin line could be an advantage since it is a more concise segmentation result. Moreover, an spatial information could be incorporated into the algorithm to eliminate the final post processing step. This would remedy the problem that the algorithm encounters when there is an object seperating the breast tissue.

Bibliography

[1]

[2] M. Abdel-Mottaleb. Automatic Segmentation, Skinline and Nipple Detection in Digital Mammograms, 1996. US Patent 5,572,565.

[3] A.L. Alexander, K. Hasan, G. Kindlmann, D.L. Parker, and J.S. Tsuruda. A Geometric Analysis of Diffusion Tensor Measurements of the Human Brain. *Magnetic Resonance in Medicine*, 44(2):283–291, 2000.

[4] A.Z. Arifin and A. Asano. Image Segmentation by Histogram Thresholding Using Hierarchical Cluster Analysis. *Pattern Recognition Letters*, 27(13):1515–1521, 2006.

[5] V. Arsigny, P. Fillard, X. Pennec, and N. Ayache. Log-Euclidean Metrics for Fast and Simple Calculus on Diffusion Tensors. *Magnetic Resonance in Medicine*, 56(2):411–421, 2006.

[6] A. Barmpoutis, M.S. Hwang, D. Howland, J.R. Forder, and B.C. Vemuri. Regularized Positive-Definite Fourth Order Tensor Field Estimation from DW-MRI. *NeuroImage*, 45(1):153–162.

[7] P.J. Basser and S. Pajevic. A Normal Distribution for Tensor-Valued Random Variables: Applications to Diffusion Tensor MRI. *IEEE Transactions on Medical Imaging*, 22(7):785–794, 2003.

[8] C. Beaulieu. The Basis of Anisotropic Water Diffusion in the Nervous System–A Technical Review. *NMR in Biomedicine*, 15(7-8):435–455, 2002.

[9] P.J. Besl and R.C. Jain. Segmentation Through Variable-Order Surface Fitting. *IEEE Transactions on Pattern Analysis and Machine Intelligence (TPAMI)*, 10(2):167–192, 1988.

[10] U. Bick, M.L. Giger, R.A. Schmidt, R.M. Nishikawa, D.E. Wolverton, and K. Doi. Automated Segmentation of Digitized Mammograms. *Academic Radiology*, 2(1):1–9, 1995.

[11] Y.Y. Boykov and M.P. Jolly. Interactive Graph Cuts for Optimal Boundary & Region Segmentation of Objects in ND Images. In *Proc of the IEEE International Conference on Computer Vision (ICCV)*, volume 1, pages 105–112, 2001.

[12] R. Chandrasekhar and Y. Attikiouzel. Gross Segmentation of Mammograms Using a Polynomial Model. In *Proc of the International Conference of the IEEE Engineering in Medicine and Biology*, volume 3, pages 1056–1058, 1996.

[13] L. Di Stefano and A. Bulgarelli. A Simple and Efficient Connected Components Labeling Algorithm. In *Proc of the International Conference on Image Analysis and Processing (ICIAP)*, page 322, 1999.

[14] S. El-Hilo, Y.T. Weldeselassie, and M.S. Atkins. Comparison Between Fourth and Second Order DT-MR Image Segmentations. In *Proc of SPIE Medical Imaging*, volume 7962, 2011.

[15] S. El-Hilo, Y.T. Weldeselassie, and M.S. Atkins. Second Order DTMR Image Segmentation Using Random Walker. In *Proc of SPIE Medical Imaging*, volume 7962, 2011.

[16] L.R. Frank. Characterization of Anisotropy in High Angular Resolution Diffusion-Weighted MRI. *Magnetic Resonance in Medicine*, 47(6):1083–1099, 2002.

[17] L. Grady. Multilabel random walker image segmentation using prior models.

[18] L. Grady. Random Walks for Image Segmentation. *IEEE Transactions on Pattern Analysis and Machine Intelligence*, pages 1768–1783, 2006.

[19] L. Jonasson, X. Bresson, P. Hagmann, O. Cuisenaire, R. Meuli, and J.P. Thiran. White Matter Fiber Tract Segmentation in DT-MRI Using Geometric Flows. *Medical Image Analysis*, 9(3):223–236, 2005.

[20] D. Le Bihan, J.F. Mangin, C. Poupon, C.A. Clark, S. Pappata, N. Molko, and H. Chabriat. Diffusion Tensor Imaging: Concepts and Applications. *Journal of Magnetic Resonance Imaging*, 13(4):534–546, 2001.

[21] C. Lenglet, M. Rousson, R. Deriche, O. Faugeras, S. Lehericy, and K. Ugurbil. A Riemannian Approach to Diffusion Tensor Images Segmentation. pages 591–602, 2005.

[22] M. Masek. Hierarchical Segmentation of Mammograms Based on Pixel Intensity. *PhD thesis, Centre for Intelligent Information Processing Systems, School of Electrical, Electronic, and Computer Engineering. University of Western Australia, Crawley, WA.*

[23] A.J. Méndez, P.G. Tahoces, M.J. Lado, M. Souto, J.L. Correa, and J.J. Vidal. Automatic Detection of Breast Border and Nipple in Digital Mammograms. *Computer Methods and Programs in Biomedicine*, 49(3):253–262, 1996.

[24] A. Oliver, X. Lladó, E. Pérez, J. Pont, E.R.E. Denton, J. Freixenet, and J. Martí. A Statistical Approach for Breast Density Segmentation. *Journal of Digital Imaging (JDI)*, pages 1–11, 2010.

[25] N. Otsu. A Threshold Selection Method from Gray-level Histograms. *Automatica*, 11:285–296, 1975.

[26] E. Ozarslan and T.H. Mareci. Generalized Diffusion Tensor Imaging and Analytical Relationships Between Diffusion Tensor Imaging and High Angular Resolution Diffusion Imaging. *Magnetic Resonance in Medicine*, 50(5):955–965, 2003.

[27] D. Raba, A. Oliver, J. Martí, M. Peracaula, and J. Espunya. Breast Segmentation With Pectoral Muscle Suppression on Digital Mammograms. *Pattern Recognition and Image Analysis*, pages 471–478, 2005.

[28] A.K. Sinop and L. Grady. A Seeded Image Segmentation Framework Unifying Graph Cuts and Random Walker Which Yields a New Algorithm. In *Proc of the IEEE International Conference on Computer Vision (ICCV)*, pages 1–8, 2007.

[29] E.A. Stamatakis, I.W. Ricketts, A.Y. Cairns, C. Walker, and P.E. Preece. Detecting Abnormalities on Mammograms by Bilateral Comparison. In *Digital Mammography*, pages 1–12, 1996.

[30] D.S. Tuch, T.G. Reese, M.R. Wiegell, N. Makris, J.W. Belliveau, and V.J. Wedeen. High Angular Resolution Diffusion Imaging Reveals Intravoxel White Matter Fiber Heterogeneity. *Magnetic Resonance in Medicine*, 48(4):577–582, 2002.

[31] Z. Wang and B.C. Vemuri. An affine invariant tensor dissimilarity measure and its applications to tensor-valued image segmentation. In *Proc of the IEEE Conference on Computer Vision and Pattern Recognition (CVPR)*, volume 1, page 228, 2004.

[32] Y.T. Weldeselassie, S. El-Hilo, and M.S. Atkins. Shape Anisotropy: Tensor Distance to Anisotropy Measure. In *Proc of SPIE Medical Imaging*, volume 7962, 2011.

[33] Y.T. Weldeselassie and G. Hamarneh. DT-MRI Segmentation Using Graph Cuts. In *Proc of SPIE Medical Imaging*, volume 6512, pages 1–9, 2007.

[34] C.F. Westin, SE Maier, H. Mamata, A. Nabavi, FA Jolesz, and R. Kikinis. Processing and Visualization for Diffusion Tensor MRI. *Medical Image Analysis*, 6(2):93–108, 2002.

[35] M.R. Wiegell, H.B.W. Larsson, and V.J. Wedeen. Fiber crossing in human brain depicted with diffusion tensor mr imaging. *Radiology*, 217(3):897, 2000.

[36] M.A. Wirth and A. Stapinski. Segmentation of the Breast Region in Mammograms Using Active Contours. In *Visual Communications and Image Processing (VCIP)*, volume 5150, pages 1995–2006, 2003.

[37] S.C. Zhu and A. Yuille. Region Competition: Unifying Snakes, Region Growing, and Bayes/MDL for Multiband Image Segmentation. *IEEE Transactions on Pattern Analysis and Machine Intelligence (TPAMI)*, 18(9):884–900, 1996.

[38] L. Zhukov, K. Museth, D. Breen, R. Whitaker, and A. Barr. Level Set Modeling and Segmentation of DT-MRI Brain Data. *Journal of Electronic Imaging*, 12(1):125–133, 2003.